NASA
Technical
Paper
3664

December 1996

X-29A Lateral–Directional Stability and Control Derivatives Extracted From High-Angle-of-Attack Flight Data

Kenneth W. Iliff
Kon-Sheng Charles Wang

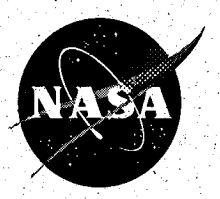

NASA Technical Paper 3664

1996

X-29A Lateral–Directional Stability and Control Derivatives Extracted From High-Angle-of-Attack Flight Data

Kenneth W. Iliff
Dryden Flight Research Center
Edwards, California

Kon-Sheng Charles Wang
SPARTA, Inc.
Lancaster, California

National Aeronautics and Space Administration

Office of Management

Scientific and Technical Information Program

CONTENTS

FIGURES

ABSTRACT

The lateral–directional stability and control derivatives of the X-29A number 2 are extracted from flight data over an angle-of-attack range of 4° to 53° using a parameter identification algorithm. The algorithm uses the linearized aircraft equations of motion and a maximum likelihood estimator in the presence of state and measurement noise. State noise is used to model the uncommanded forcing function caused by unsteady aerodynamics over the aircraft at angles of attack above 15°. The results supported the flight-envelope-expansion phase of the X-29A number 2 by helping to update the aerodynamic mathematical model, to improve the real-time simulator, and to revise flight control system laws. Effects of the aircraft high gain flight control system on maneuver quality and the estimated derivatives are also discussed. The derivatives are plotted as functions of angle of attack and compared with the predicted aerodynamic database. Agreement between predicted and flight values is quite good for some derivatives such as the lateral force due to sideslip, the lateral force due to rudder deflection, and the rolling moment due to roll rate. The results also show significant differences in several important derivatives such as the rolling moment due to sideslip, the yawing moment due to sideslip, the yawing moment due to aileron deflection, and the yawing moment due to rudder deflection.

NOMENCLATURE

Acronyms

AFB	Air Force Base
AFFTC	Air Force Flight Test Center, Edwards Air Force Base, California
ARI	aileron-to-rudder interconnect
DFRC	Dryden Flight Research Center (formerly Dryden Flight Research Facility)
DOF	degree of freedom
FCS	flight control system
FSW	forward-swept wing
INS	inertial navigation system
MAC	mean aerodynamic chord
NACA	National Advisory Committee for Aeronautics
PID	parameter identification
TED	trailing-edge down
TEU	trailing-edge up
USAF	United States Air Force

Symbols

A, B, C, D, F, G	system matrices
C_{l_β}	coefficient of rolling moment due to sideslip, deg^{-1}
C_{n_β}	coefficient of yawing moment due to sideslip, deg^{-1}

C_{Y_β}	coefficient of lateral force due to sideslip, deg^{-1}
$C_{l_{\delta_a}}$	coefficient of rolling moment due to differential aileron deflection, deg^{-1}
$C_{n_{\delta_a}}$	coefficient of yawing moment due to differential aileron deflection, deg^{-1}
$C_{Y_{\delta_a}}$	coefficient of lateral force due to differential aileron deflection, deg^{-1}
$C_{l_{\delta_r}}$	coefficient of rolling moment due to rudder deflection, deg^{-1}
$C_{n_{\delta_r}}$	coefficient of yawing moment due to rudder deflection, deg^{-1}
$C_{Y_{\delta_r}}$	coefficient of lateral force due to rudder deflection, deg^{-1}
C_{l_p}	coefficient of rolling moment due to roll rate, rad^{-1}
C_{l_r}	coefficient of rolling moment due to yaw rate, rad^{-1}
C_{n_p}	coefficient of yawing moment due to roll rate, rad^{-1}
C_{n_r}	coefficient of yawing moment due to yaw rate, rad^{-1}
C_{l_0}	rolling moment bias
C_{n_0}	yawing moment bias
C_{Y_0}	lateral force bias
f	system state function
$\mathbf{GG}^*$	measurement noise covariance matrix
g	system observation function
$\mathbf{H}$	approximation to information matrix
J	cost function
L	iteration number
N	number of time points
$\mathbf{n}$	state noise vector
$\mathbf{R}$	innovation covariance matrix
t	time, sec
$\mathbf{u}$	known control input vector
$\mathbf{x}$	state vector
$\dot{\mathbf{x}}$	time derivative of state vector

$\tilde{\mathbf{x}}_\xi$	predicted state estimate
$\mathbf{z}$	observation vector
$\tilde{\mathbf{z}}_\xi$	predicted Kalman filter estimate
δ_a	aileron (flaperon) deflection, $\delta_a = (0.5)\delta_{a_{left}} - (0.5)\delta_{a_{right}}$, deg
δ_r	rudder deflection, deg
η	measurement noise vector
ξ	unknown parameter vector
$\hat{\xi}$	estimate of ξ
Φ	transition matrix
ψ	integral of transition matrix
∇_ξ	gradient with respect to ξ

INTRODUCTION

The X-29A advanced technology demonstrator program was conducted between 1984 and 1992 at the NASA Dryden Flight Research Facility,* Edwards, California. During these 8 years of flight research, many unique and important results on flight dynamics, transonic aerodynamics, aerostructures, composite materials, airfoil technology, and aircraft stability and control were explored.

The Grumman Aerospace Corporation designed and built two X-29A airplanes in the early 1980s under a contract sponsored by the Defense Advanced Research Projects Agency and funded through the United States Air Force (USAF). These aircraft incorporated a forward-swept wing (FSW), close-coupled canard, lightweight fighter design. The prime flight research objective was to test the predicted aerodynamic advantages of the unique FSW configuration and its unprecedented level of static instability for an airplane. Compared with conventional straight or aft-swept wings, a FSW configuration offers better control at high angles of attack (AOA), allowing the aircraft to be more departure resistant and, in particular, maintain significant roll control at extreme AOA. Phenomenologically, these capabilities are achievable because the typical stall pattern of an aft-swept wing, from wingtip to root, is reversed for a FSW, which stalls from root to tip.

The first X-29A verified the predicted benefits of the innovative technologies on board and performed limited envelope expansion to 22.5° AOA and to Mach 1.48. Additional work evaluated handling qualities, military utility, and agility. The second X-29A incorporated hardware and software modifications to allow low-speed, high-AOA flight, with demonstrated pitch-pointing to 67° AOA. In addition to fundamental flowfield studies at high AOA, all-axis maneuverability and controllability to approximately 45° AOA was investigated for military purposes.

*The current name is NASA Dryden Flight Research Center (DFRC). In the rest of this paper, this center is referred to as DFRC although some of the work was performed while it was known as a facility.

This technical paper focuses on aerodynamic parameter identification (PID) performed for the X-29A number 2 at high angles of attack. During flights 6 to 30 from October 1989 to March 1990 and flights 117, 118, and 120 in September 1991, several maneuvers were performed to provide data for aircraft PID, the results of which supported the high-AOA envelope expansion phase. Reported here are lateral–directional stability and control derivatives extracted from 52 flight maneuvers using a specialized parameter estimation program developed at DFRC. The estimator accounts for state (process) and observation (measurement) noise. State noise is used to model the uncommanded forcing function resulting from separated and vortical flows over the aircraft above 15° AOA. Derivatives between 4° and 53° AOA are estimated, plotted, and discussed in relation to the predicted aerodynamic database and the quality of the PID maneuvers.

Use of trade names or names of manufacturers in this document does not constitute an official endorsement of such products or manufacturers, either expressed or implied, by the National Aeronautics and Space Administration.

FLIGHT PROGRAM OVERVIEW

High-AOA flight testing of the second X-29A was a follow-on to the successful flight testing of the first X-29A, which performed 242 research flights between December 1984 and December 1988 (refs. 1 and 2). These flights proved the integrated viability of several advanced technologies involving aerodynamics, structures, materials, and flight controls (refs. 3, 4, and 5). During this time, the flight envelope was expanded up to Mach 1.48, just above 50,000 ft, and up to 22.5° AOA in subsonic flight.

The second X-29A (fig. 1) investigated the low-speed, very high AOA aerodynamics and flight dynamics of the airplane (refs. 6 and 7). Flight control system (FCS) modifications to this aircraft were designed by DFRC and the Air Force Flight Test Center (AFFTC), while airplane modifications were made by the Grumman Aerospace Corporation (see section entitled "Vehicle Description"). Four general phases made up the high-AOA flight test program: (1) functional check flights, (2) envelope expansion, (3) military utility evaluation, and (4) aerocharacterization. These four phases spanned 120 flights between May 1989 and September 1991. (An additional 60 flights conducted by the USAF between May and August 1992 comprised a USAF study of forebody vortex flow control.)

Functional check flights were completed in the first five flights, performed primarily to evaluate the aircraft's systems, low-AOA flight controls, engine, and aeroservoelastic stability. During this phase, a spin parachute system added by Grumman was deployed twice in flight under controlled conditions to verify its operation. In addition, airdata calibrations and pilot proficiency maneuvers were accomplished. Envelope expansion flights were performed during the second phase to probe the aircraft's high-AOA limits and to clear the aircraft to maneuver through as large an envelope as possible. This phase of testing took place from flights 6 to 85. Investigations of military utility and high-AOA flying qualities were phased in at flight 45 and ran through flight 120. Aerocharacterization flights— which studied the strong vortical flowfield of the X-29A forebody above 15° AOA—took place between flights 86 and 120, overlapping the tactical utility (third) phase.

Envelope expansion for X-29A number 2 was accomplished through a carefully planned buildup approach (see the section titled "Predictions and Envelope Expansion Methods") using a well-documented high-AOA database established from wind-tunnel results, radio-controlled subscale drop model results, a six-degree-of-freedom (DOF) computer simulation aerodynamic model, and X-29A

number 1 flight data below 22.5° AOA. High-AOA capabilities were demonstrated with positive and precise pitch-pointing to 67° AOA, all-axis maneuvering to 45° AOA at 1 *g*, and 35° AOA stabilized flight at airspeeds up to 300 knots. Lateral–directional control was available throughout the flight envelope up to 45° AOA, with degradation occurring gradually at higher AOA; no sudden loss of control was observed. Longitudinal flying qualities were reported good up to 50° AOA.

DFRC operated the X-29A advanced technology demonstrator as the responsible test organization. Participating test organizations included the AFFTC and Grumman. The Air Force Wright Laboratory was responsible for program management through its Flight Dynamics Directorate.

The final research flight of the X-29A program was made by the number 2 aircraft on August 28, 1992. At the time of this writing, X-29A number 1 was dispositioned to the USAF Museum at Wright-Patterson AFB, Dayton, Ohio, and X-29A number 2 was on static display at DFRC.

VEHICLE DESCRIPTION

The X-29A advanced technology demonstrator is a single-seat, single-engine, fighter-class aircraft that integrates several advanced technologies intended to enhance aircraft performance and maneuverability, especially in transonic flight and at high angles of attack. Though the most noteworthy feature of the airplane is its FSW, several other innovative features are significant, including the following:

- Thin supercritical airfoil.
- Aeroelastically tailored composite wing structure.
- Close-coupled, variable incidence canards.
- Relaxed static stability.
- Triply redundant digitial fly-by-wire flight control system (FCS).
- Automatic variable wing camber control.
- Three-surface longitudinal (pitch) control.

Figure 2 shows a three-view layout of the aircraft with major geometrical characteristics. The X-29A is a relatively small aircraft, with a length of 48.1 ft, wing span of 27.2 ft, and height of 14.3 ft. Gross takeoff weight of the aircraft is approximately 18,000 lb, which includes a fuel weight of approximately 4,000 lb. References 8 and 9 provide more extensive dimensional data.

The design of the X-29A used flight-proven, off-the-shelf equipment and systems wherever possible to minimize cost, development time, and technical risks. This included the forebody and cockpit from a Northrop F-5A aircraft; flight instrumentation from a Grumman F-14 aircraft; main landing gear, emergency power unit, jet fuel starter, and actuators from a General Dynamics F-16 aircraft; a General Electric F404-GE-400 engine with afterburner from a McDonnell-Douglas F/A-18 aircraft; and Honeywell HDP5301 flight control computers from a Lockheed SR-71 aircraft.

The unique design of the X-29A features a 4.9 percent thin, supercritical, 29.3° FSW with no leading-edge devices; close-coupled canard; and three-surface pitch control (ref. 10). The three-surface pitch control uses the close-coupled canard, the full-span wing flaperon, and small strake flaps at the rear of the

aircraft. Operated differentially, the full-span, double-hinged, variable camber flaperons also provide lateral control. These flaperons provide all roll control, as the configuration does not use spoilers, rolling tail, or differential canards. A conventional rudder mounted on a fixed vertical stabilizer provides directional control. The left and right canards are driven symmetrically and operate at a maximum rate of approximately 100°/sec through a range of 60° trailing-edge up (TEU) and 30° trailing-edge down (TED). The wing flaperons move at a maximum rate of 68°/sec through a range of 10° TEU and 25° TED. The rudder has a range of ±30° and a maximum rate of 141°/sec. The strake flaps also act within a range of ±30° but have a maximum rate of only 27°/sec. The aircraft is statically unstable in the longitudinal axis, with a negative static margin of up to 35 percent at subsonic speeds. In the supersonic regime approaching Mach 1.4, the aircraft exhibits near-neutral stability.

Several other important vehicle features are noteworthy. The wing structure consists of aeroelastically tailored graphite-epoxy covers bolted to aluminum and titanium spars to provide adequate stiffness against the natural structural tendency of the FSW configuration toward torsional divergence. The fuselage cross-section was area-ruled for good high-speed performance, especially in the transonic regime. A single General Electric F404-400 engine provides 16,000 lb of thrust. Two side-mounted, fixed geometry (simple bifurcated) inlets feed the engine. A triplex, digital, FCS is incorporated using an analog backup. The digital control law outputs are run at 40 Hz on Honeywell 5301 dual-processor flight computers (ref. 11). Unlike the first X-29A (USAF SN 20003), the second aircraft (SN 20049) has no wing surface static pressure ports, wing deflection measurement devices, or calibrated structural loads instrumentation. Other than the following high-AOA modifications made to the second X-29A, the two aircraft have the same configuration.

- A mortar-deployed and manually jettisoned spin recovery parachute system.
- Two additional noseboom angle-of-attack vanes for flight-control sensor redundancy.
- A Litton LN-39 inertial navigation system (INS) to provide information for computing AOA, sideslip, and other airdata parameters at high AOA for postflight analysis.
- Modified emergency power unit and environmental control system for high-AOA suitability.
- Additional cockpit instrumentation for high-AOA testing: large-AOA and yaw-rate gauges, a single-needle altimeter, spin chute controls and status displays, and spin-recovery lights.
- Ports to measure surface pressure distribution at four forebody fuselage stations, added during phase 4 aerocharacterization flights (ref. 12).

Software modifications were also made to the FCS of the second X-29A for improved high-AOA flying qualities, departure resistance, and spin prevention. The revised Block 9AA-01 control laws were designed at DFRC by a combined effort with the AFFTC. The longitudinal axis required little modification from the low-AOA system originally designed by Grumman for the first X-29A.

> "The [longitudinal] control laws were basically a pitch rate command system with a weak AOA feedback to provide positive apparent speed stability to the pilot via increased aft stick force requirements at AOA. Gravity vector compensation to the pitch rate command was removed above 15° AOA to avoid redundancy management problems with the single string nature of the Attitude Heading Reference System (AHRS). Negative AOA and load factor limiters were also incorporated to aid in preventing large negative AOA." (ref. 13)

The lateral–directional control system required extensive modifications to provide adequate performance above 15° AOA. Changes included:

- Increased gain roll damper using pure roll-rate (aileron) feedback.
- Elimination of the low-AOA lateral integrator to prevent tendency for control surface saturation.
- Washed-out stability axis yaw-rate feedback to the rudder.
- Aileron-to-rudder interconnect (ARI), which incorporated a parallel wash-out path to provide extra initial kick for roll coordination.
- Extensive AOA and airspeed gain scheduling.
- Spin prevention logic with pilot override capability.

Below 10° AOA, the flight control laws were identical to the Block 8AD software release flown in the first X-29A in late 1988. Lateral–directional, high-AOA control laws blended in between 10° and 15° AOA, and the longitudinal high-AOA control laws were faded in between 15° and 20°. References 6, 9, 10, and 14 give further details on the design and development of the high-AOA control laws.

For accurate flightpath targeting, an uplink system (ref. 15) was employed to provide the capability to drive the horizontal and vertical flightpath command needles in the cockpit attitude direction indicator. These needles, which were proportional to the error between target and measured AOA and angle of sideslip, helped the pilot capture and hold precise test points, especially during high-AOA maneuvers. The pilots were able to concentrate on a single instrument to receive attitude, AOA, and sideslip information. This uplink targeting system proved useful for the stability and control PID maneuvers discussed in this paper.

The upper surface of the right wingtip and the left side of the vertical stabilizer tip have stripes painted on them. Besides being another feature distinguishing it from the first X-29A, the stripes were added in case a spin necessitated aircraft orientation identification from long-range optics.

INSTRUMENTATION AND DATA ACQUISITION

Airdata issues were carefully considered as such data constituted a primary source of research information. For example, measurement of accurate AOA was important as (1) a primary gain scheduling parameter for the FCS, (2) a feedback to both longitudinal and lateral–directional axes, and (3) a basic input for postflight maneuver analysis and PID. In addition, this paper uses AOA as the correlating variable to compare model-predicted and flight-extracted stability and control derivatives.

A standard National Advisory Committee for Aeronautics (NACA) 6-ft noseboom was used to measure AOA, angle of sideslip, and total and static pressure, from which velocity and altitude could be computed. Impact pressure was measured with two independent sensors in the noseboom pitot probe. Two fuselage-mounted AOA sensors, one on each side of the airplane, had ranges limited to 35° AOA. Because their location and range were considered inadequate for accuracy, two additional AOA vanes were mounted on the noseboom just aft of the main AOA vane. A pair of heated, fuselage-mounted, pitot-static probes was available for redundancy to the noseboom probe, though these were expected to

have poor characteristics at high AOA. A heated, total temperature probe was located on the underside of the airplane, just forward of the nosewheel.

Because measurements from the total pressure and total temperature probes began to attenuate above 30° AOA, an INS was installed in the airplane to augment airdata measurements at high AOA (ref. 16). INS-provided data were only used for postflight analysis, not as inputs to the FCS. The INS provided three components of ground-referenced velocity and three aircraft Euler angles. The velocity and attitude data were then used to compute AOA, sideslip, dynamic pressure, true airspeed, and Mach number. Accurate dynamic pressure was needed to compute nondimensionalized force and moment coefficients and the stability and control derivatives presented later in this paper.

Flight instrumentation also included a set of three-axis angular accelerometers. Angular rates were measured using three-axis rate gyros. Linear accelerations were determined from a body-mounted, three-axis accelerometer system. Control surface positions were measured using control position transducers.

The above flight dynamics measurements were corrected before their use as inputs for parameter identification. Corrections were applied to the airspeed data to obtain true velocity, Mach number, and dynamic pressure. True noseboom vane-indicated AOA and sideslip were determined by applying corrections for upwash and noseboom bending. Measurements of linear acceleration, AOA, and angle of sideslip were corrected (in the PID program) for displacement from the center of gravity. Mass and inertial characteristics were computed using calibrated real-time fuel quantities.

Because vehicle space was limited, there was no on-board data recording system. All data were transmitted to the ground for recording, real-time analysis, and control-room monitoring. Sensor outputs were preprocessed by appropriate signal conditioning units and then sampled (at rates ranging from 25 to 400 Hz) by a five-module, 10-bit pulse code modulation system. Longitudinal acceleration, lateral acceleration, and normal acceleration were filtered with a second-order, notch-filtering technique with a frequency of 68 rad/sec. The remaining data were filtered using a low-pass, digital filter with a break frequency of 15 Hz. Combined with a constant-bandwidth frequency modulation system, the signals were then encoded and transmitted to ground telemetry stations. For the present PID analysis, the stability and control data were thinned to a final sample rate of 40 Hz.

Furthermore, the data were corrected for time lags introduced by sensor dynamics and the aforementioned signal filtering before analysis of the dynamic stability and control maneuvers was performed. The importance of making these corrections to obtain adequate estimates of the stability and control derivatives cannot be overstated (ref. 17).

PREDICTIONS AND ENVELOPE EXPANSION METHODS

Experimental predictions of high-AOA aerodynamics and flight dynamics were developed for the X-29A configuration through a series of subscale model tests. These included static wind-tunnel tests (ref. 18), free-flight (dynamic) wind-tunnel tests (ref. 19), vertical (spin) tunnel tests (ref. 20), rotary balance tests (ref. 21), and airborne drop-model tests (refs. 22 and 23). Early X-29A predicted high-AOA aerodynamics are reviewed by Grafton et al. (ref. 24).

Data from these tests were used jointly by Grumman and NASA Langley Research Center to build, respectively, the longitudinal and lateral–directional portions of a high-AOA aerodynamic math model. Grumman integrated the results and included additional rotary balance data (ref. 25) and corrections to

rudder, aileron, and negative AOA data to create a nonlinear, six degree-of-freedom aerodynamic math model known as AERO9B (ref. 26), released by Grumman in July 1988. The baseline model, which contained more than 3000 lines of FORTRAN 77 code and data tables with over 100,000 data points, was available between –50° and 90° AOA and ±30° angle of sideslip. At DFRC, the aero model was used in both the piloted real-time simulator and also in batch simulations for flight data analysis. In addition, an aerodynamic parameter variation study (ref. 6) was conducted using the DFRC simulator, yielding important information on departure characteristics, identification of critical aerodynamic parameters, and definition of real-time flight limits.

The flight envelope of the second X-29A was expanded cautiously and incrementally, starting with relatively benign inputs and low AOA and progressing to larger amplitude and higher AOA maneuvers. Specific maneuvers and pilot inputs were chosen based on their ability to produce sufficient aircraft motion for subsequent parameter identification. Pilots were trained to fly the maneuvers by practicing in the X-29A ground-based simulator, manually inputting aileron and rudder inputs to adequately stimulate the aircraft response. Later, in actual flight, the pilot would fly these maneuver sets at predetermined flight conditions, with pilot-commanded aileron and rudder pulses and aircraft motions recorded for post-flight analysis.

An analysis of the flight maneuvers using the PID method discussed in the next section yielded flight-determined aerodynamic stability and control derivatives. The differences between flight-determined and model-predicted derivatives were identified and assembled in a "delta file." This delta file was then added to the baseline AERO9B math model to create an updated aerodynamic database. This procedure proved to be a very useful and efficient means of updating an otherwise highly complex aeromodel. The updated model was independently checked against flight data, and further adjustments were made to the delta file as necessary until the correspondence between model and flight was adequate. The modified delta file was then copied to the real-time simulator for pilot evaluation. Combined with sound engineering judgment and experience, these estimation efforts formed the basis for updating the aeromodel database. References 8 and 26 fully describe the development and actual implementation of these aero deltas into the X-29A number 2 simulator and FCS. These references also include the final deltas used in the X-29A flight program. Since such files are a direct measure of the differences between prediction and flight, they also provide an evaluation of the predictive techniques used to design the aircraft.

Determination of the next test point for envelope expansion relied on simulation results from the updated aerodynamic model, as well as on predictions, trends, and previous high-AOA experience. After flight, differences between flight-determined and model-predicted derivatives would again be used to update the delta file to further improve the simulation model. This incremental process, contingent on the updated model being representative of the latest flight data set, would proceed with higher and higher AOA and sideslip until the entire flight envelope was explored. All maneuvers analyzed for PID were flown with the aircraft's FCS (as described in the "Vehicle Description" section) engaged; disengagement of the FCS would lead to departure of the statically unstable aircraft. Reference 27 presents other PID methods and results for the second X-29A. References 6, 13, and 28 report additional details on the prediction and expansion methods used to support PID for the second X-29A.

PARAMETER IDENTIFICATION METHODOLOGY

The purpose of the X-29A number 2 flight program was to evaluate the aircraft configuration at high AOA. Those familiar with aircraft know that at AOA where significant separated and vortical flows

occur, the aircraft exhibits uncommanded motions. The present aircraft is no exception. Reference 29 discusses maneuver difficulties and related analysis issues under these conditions, using the 3/8-scale F-15 Remotely Piloted Vehicle aircraft from –20° to 53° AOA. The uncommanded motions vary from relatively small high-frequency disturbances, to very large wing rocking motions, to complete roll-off from the flight condition. In addition to being bothersome to the pilot, these uncommanded motions also complicate the extraction of stability and control derivatives from the planned stability and control maneuvers (ref. 29). The difficulty of the analysis is also increased by the high gain FCS of the X-29A number 2 necessarily being engaged for all PID maneuvers flown. To better understand these maneuvers, the authors found it necessary to account for the uncommanded portions of the aircraft motion.

The procedure in this analysis uses state noise to model the uncommanded forcing function. References 30, 31, and 32 completely describe this technique. The procedure also uses small perturbation analysis and requires that the normal six degree-of-freedom aircraft equations of motion be linear in the aerodynamic coefficients. This requirement presents no particular mathematical difficulty because the normal stability and control derivatives are already locally linear approximations of nonlinear aircraft aerodynamics.

To perform the analysis presented here, an existing PID (estimation) computer program was modified to account properly for the additional complexity involved by including the effects of state noise (commands resulting from separated flow) on the stability and control maneuvers. A brief description of the state noise algorithm follows.

Making a precise, mathematically probabilistic statement of the parameter estimation problem is possible. The first step is to define the general system model (aircraft equations of motion). This model can be written in the continuous/discrete form as

$$\mathbf{x}(t_0) = \mathbf{x}_0 \tag{1}$$

$$\dot{\mathbf{x}}(t) = f[\mathbf{x}(t), \mathbf{u}(t), \xi] + \mathbf{F}(\xi)\mathbf{n}(t) \tag{2}$$

$$\mathbf{z}(t_i) = g[\mathbf{x}(t_i), \mathbf{u}(t_i), \xi] + \mathbf{G}(\xi)\eta_i \tag{3}$$

where $\mathbf{x}$ is the state vector, $\mathbf{z}$ is the observation vector, f and g are system state and observation functions, $\mathbf{u}$ is the known control input vector, ξ is the unknown parameter vector, $\mathbf{n}$ is the state noise vector, η is the measurement noise vector, $\mathbf{F}$ and $\mathbf{G}$ are system matrices, and t is time. The state noise vector is assumed to be zero-mean white Gaussian and stationary, and the measurement noise vector is assumed to be a sequence of independent Gaussian random variables with zero mean and identity covariance. For each possible estimate of the unknown parameters, a probability that the aircraft response time histories attain values near the observed values can then be defined. The maximum likelihood estimates are defined as those that maximize this probability. Maximum likelihood estimation has many desirable statistical characteristics; for example, it yields asymptotically unbiased, consistent, and efficient estimates.

If there is no state noise and the matrix $\mathbf{G}$ is known, then the maximum likelihood estimator minimizes the cost function

$$J(\xi) = \frac{1}{2}\sum_{i=1}^{N}[\mathbf{z}(t_i)-\tilde{\mathbf{z}}_\xi(t_i)]^*(\mathbf{G}\mathbf{G}^*)^{-1}[\mathbf{z}(t_i)-\tilde{\mathbf{z}}_\xi(t_i)] + \frac{1}{2}N\ln|(\mathbf{G}\mathbf{G}^*)| \tag{4}$$

where $\mathbf{GG}^*$ is the measurement noise covariance matrix, and $\tilde{\mathbf{z}}_\xi(t_i)$ is the computed response estimate of $\mathbf{z}$ at t_i for a given value of the unknown parameter vector ξ, and N is the number of time points. The cost function is a function of the difference between the measured and computed time histories.

If equations (2) and (3) are linearized (as is the case for the stability and control derivatives in the aircraft problem), then

$$\mathbf{x}(t_0) = \mathbf{x}_0 \tag{5}$$

$$\dot{\mathbf{x}}(t) = \mathbf{A}\mathbf{x}(t) + \mathbf{B}\mathbf{u}(t) + \mathbf{F}\mathbf{n}(t) \tag{6}$$

$$\mathbf{z}(t_i) = \mathbf{C}\mathbf{x}(t_i) + \mathbf{D}\mathbf{u}(t_i) + \mathbf{G}\eta_i \tag{7}$$

where $\mathbf{A}$, $\mathbf{B}$, $\mathbf{C}$, and $\mathbf{D}$ are system matrices. For the no-state-noise case, the $\tilde{\mathbf{z}}_\xi(t_i)$ term of equation (4) can be approximated by

$$\tilde{\mathbf{x}}_\xi(t_0) = \mathbf{x}_0(\xi) \tag{8}$$

$$\tilde{\mathbf{x}}_\xi(t_{i+1}) = \Phi\tilde{\mathbf{x}}_\xi(t_i) + \psi[\mathbf{u}(t_i) + \mathbf{u}(t_{i+1})]/2 \tag{9}$$

$$\tilde{\mathbf{z}}_\xi(t_i) = \mathbf{C}\tilde{\mathbf{x}}_\xi(t_i) + \mathbf{D}\mathbf{u}(t_i) \tag{10}$$

where the transition matrix, Φ, and the integral of the transition matrix, ψ, are given by

$$\Phi = \exp[A(t_{i+1} - t_i)] \tag{11}$$

$$\psi = \int_{t_i}^{t_{i+1}} \exp(\mathbf{A}\tau)d\tau\mathbf{B} \tag{12}$$

When state noise is important (as implemented here to model uncommanded aircraft motions), the nonlinear form of equations (1) to (3) is intractable. For the linear model defined by equations (5) to (7), the cost function that accounts for state noise is

$$J(\xi) = \frac{1}{2}\sum_{i=1}^{N} [\mathbf{z}(t_i) - \tilde{\mathbf{z}}_\xi(t_i)]^*\mathbf{R}^{-1}[\mathbf{z}(t_i) - \tilde{\mathbf{z}}_\xi(t_i)] + \frac{1}{2}N\ln|\mathbf{R}| \tag{13}$$

where $\mathbf{R}$ is the innovation covariance matrix. The $\tilde{\mathbf{z}}_\xi(t_i)$ term in equation (13) is the Kalman-filtered estimate of $\mathbf{z}$, which, if the state noise covariance is zero, reduces to the form of equation (4). If there is no state noise, the second term of equation (13) is of no consequence (unless one wishes to include elements of the $\mathbf{G}$ matrix), and $\mathbf{R}$ can be replaced by $\mathbf{GG}^*$, which makes equation (13) the same as equation (4).

To minimize the cost function $J(\xi)$, we can apply the Newton-Raphson algorithm, which chooses successive estimates of the vector of unknown coefficients, $\hat{\xi}$. Let L be the iteration number. The $L + 1$ estimate of $\hat{\xi}$ is then obtained from the L estimate as follows:

$$\hat{\xi}_{L+1} = \hat{\xi}_L - [\nabla_\xi^2 J(\hat{\xi}_L)]^{-1}[\nabla_\xi^* J(\hat{\xi}_L)] \tag{14}$$

If **R** is assumed fixed, the first and second gradients are defined as

$$\nabla_\xi J(\xi) = -\sum_{i=1}^{N} [\mathbf{z}(t_i) - \tilde{\mathbf{z}}_\xi(t_i)]^* (\mathbf{G}\mathbf{G}^*)^{-1} [\nabla_\xi \tilde{\mathbf{z}}_\xi(t_i)] \tag{15}$$

$$\begin{aligned} \nabla_\xi^2 J(\xi) = & \sum_{i=1}^{N} [\nabla_\xi \tilde{\mathbf{z}}_\xi(t_i)]^* (\mathbf{G}\mathbf{G}^*)^{-1} [\nabla_\xi \tilde{\mathbf{z}}_\xi(t_i)] \\ & - \sum_{i=1}^{N} [\mathbf{z}(t_i) - \tilde{\mathbf{z}}_\xi(t_i)]^* (\mathbf{G}\mathbf{G}^*)^{-1} [\nabla_\xi^2 \tilde{\mathbf{z}}_\xi(t_i)] \end{aligned} \tag{16(a))}$$

The Gauss-Newton approximation to the second gradient is

$$\nabla_\xi^2 J(\xi) \cong \sum_{i=1}^{N} [\nabla_\xi \tilde{\mathbf{z}}_\xi(t_i)]^* (\mathbf{G}\mathbf{G}^*)^{-1} [\nabla_\xi \tilde{\mathbf{z}}_\xi(t_i)] \tag{16(b))}$$

The Gauss-Newton approximation, which in previous reports was sometimes referred to as modified Newton-Raphson, is computationally much easier than the Newton-Raphson approximation because the second gradient of the innovation never needs to be calculated.

Figure 3 illustrates the maximum likelihood estimation concept. The measured response is compared with the estimated response, and the difference between these responses is called the response error. The cost functions of equations (4) and (13) includes this response error. The minimization algorithm is used to find the coefficient values which minimize the cost function. Each iteration of this algorithm provides a new estimate of the unknown coefficients on the basis of the response error. These new estimates are then used to update values of the coefficients of the mathematical model, providing a new estimated response and, therefore, a new response error. Updating of the mathematical model continues iteratively until a predetermined convergence criterion is satisfied. The estimates resulting from this procedure are the maximum likelihood estimates.

The maximum likelihood estimator also provides a measure of the reliability of each estimate based on the information obtained from each dynamic maneuver. This measure of the reliability, analogous to the standard deviation, is called the Cramér-Rao bound (refs. 31 and 33). The Cramér-Rao bound, as computed by the current program, generally should be used as a measure of relative rather than absolute accuracy. The bound is obtained from the approximation to the information matrix, **H**, which is based on equation (16(b)); the actual information matrix is defined when evaluated at the correct values (not the maximum likelihood estimates) of all the coefficients. The bound for each unknown is the square root of the corresponding diagonal element of $\mathbf{H}^{-1}$; that is, for the ith unknown, the Cramér-Rao bound is $\sqrt{(\mathbf{H}^{-1})_{i,i}}$. The stability and control derivatives above 15° AOA that are presented in the next section were analyzed assuming that state noise was present.

RESULTS AND DISCUSSION

The stability and control maneuvers examined here were analyzed with the estimation method described in the previous section. All 52 maneuvers were performed at subsonic, 1-g flight conditions. Ten maneuvers were below 15° AOA; these did not exhibit uncommanded motions from flow anomalies and were, therefore, analyzed without assuming state noise. Equations 8 through 10 were applied. The remaining 42 maneuvers above 15° AOA were analyzed assuming state noise effects, requiring the cost function accounting for state noise (equation 13) to be minimized.

Figure 4 shows the time history of a typical, high-AOA, lateral–directional, PID maneuver. Figure 4(a) shows the flight conditions of the 15-sec maneuver with 36.5° ± 1.0°AOA, altitude 34,500 to 32,500 ft, Mach number 0.31 ± 0.01, and dynamic pressure 36 ± 3 lb/ft^2. The parameters and their variations are typical for high angle-of-attack PID maneuvers for the X-29A and most other aircraft. Figure 4(b) gives the input and response signals used for PID. The highest frequencies exhibited result from overall vibration of the sensors; the frequencies near 1 to 2 Hz result from separated and vortical flows at high AOA; and the frequencies below 1 Hz result from a combination of aircraft dutch-roll, pilot control input, and the still present separated and vortical flows.

Figure 4(c) illustrates some postflight analysis problems associated with using the X-29A high gain feedback control system. The portions of the time history where roll rate is out of phase with negative aileron result from the pilot aileron doublet input, and the portions where roll rate and negative aileron in phase result from a combination of the high gain control system and some additional pilot input against the roll rate. The high correlation between the nondoublet portion of the maneuver along with the uncommanded roll motion for aileron and roll rate makes the separation of the effects due to aileron and roll rate difficult to assess. Figure 4(d) shows the effect of the ARI. Aileron and rudder responses are shown along with the pilot rudder doublet inputs. At 0, 6, and 9 sec, the rudder exhibits motions that are not caused by rudder pedal input but are closely correlated with aileron motion. These additional rudder motions result from the ARI as specified in the feedback control system. The effect of this interconnect over large portions of the maneuver makes it difficult to separate the aileron effect on the aircraft from the rudder and rate effects. To sum up, figure 4 illustrates some of the difficulties in identifiability of the control and rate effects for the X-29A number 2, attributable to its high gain control system as well as to uncommanded responses caused by unsteady separated and vortical flows.

Figures 5 through 9 present the estimates of the derivatives determined in the PID analysis. These include C_{l_β}, C_{n_β}, C_{Y_β}, $C_{l_{\delta_a}}$, $C_{n_{\delta_a}}$, $C_{Y_{\delta_a}}$, $C_{l_{\delta_r}}$, $C_{n_{\delta_r}}$, $C_{Y_{\delta_r}}$, C_{l_p}, C_{l_r}, C_{n_p}, C_{n_r}, C_{l_0}, C_{n_0}, and C_{Y_0}. Each derivative is plotted as a function of AOA, where the circle symbols are the flight estimates, the vertical lines are the uncertainty levels, and the dashed line is the fairing of predicted values from the wind-tunnel-derived AERO9B simulation database (refs. 26 and 28). The uncertainty levels (ref. 17) shown on the plots are obtained by multiplying the Cramér-Rao bound of each estimate by a factor of 3. The solid fairing is the authors' interpretation of the flight data over the entire AOA range, based on uncertainty levels, the scatter of adjacent estimates around a given AOA, and engineering judgment of the maneuver quality. Theoretically, information on maneuver quality such as the length of the maneuver, amount of control input, excitation of the response variables (slideslip, roll rate, yaw rate, and lateral acceleration),

and correlation between control motions is contained in the value of the uncertainty level. A large uncertainty level indicates low information on the derivative estimate for that maneuver, and a small uncertainty level indicates high information.

Reynolds number effects are known to cause differences between wind-tunnel predictions and flight results, especially where vortex flows are dominant. The Reynolds numbers for the flight data examined here are between 5 and 6 million and are nearly an order of magnitude larger than the Reynolds numbers for most of the wind-tunnel tests.

Three maneuvers are included above 50° AOA (51.3°, 52.7°, and 52.8°). For several reasons, analysis of these maneuvers provided estimates that are somewhat less reliable than those at lower AOA values. The estimates are obtained in an AOA region where the vehicle has a strong tendency to exhibit uncommanded yaw rates. The variation of yawing moment plus activation of the spin suppression system and various interconnects make the maneuvers difficult to analyze. These three maneuvers were analyzed with the $C_{l_{\delta_r}}$, $C_{n_{\delta_r}}$, and $C_{Y_{\delta_r}}$ derivatives set to zero. This setting is supported because analysis below 50° AOA indicated that the rudder derivatives were essentially zero at 50° AOA, as figure 7 shows.

The estimation of stability and control derivatives at high AOA is always difficult because of the uncertainty of the aerodynamic mathematical model and the occurrences of uncommanded responses during the dynamic maneuvers as indicated earlier. The estimation process is further complicated for the X-29A number 2 because the maneuvers were obtained with the high gain control system engaged, which resulted in smaller excursions, artificially highly damped responses, and high correlation between the responses and the control motions (fig. 4). The impact of these complications results in very little independence between the control derivatives and the damping derivatives. This near-derivative dependence (ref. 17) was the reason a small *a priori* weighting (ref. 33) was used on the damping derivatives (see the section "Rotary Derivatives").

Sideslip Derivatives

The agreement in figure 5(a) between the predicted and flight-determined C_{l_β} (dihedral) is good below 7° AOA. The flight data show more scatter and larger uncertainty levels above 18° AOA with values varying between –0.002 and –0.004 and the predominant trend showing a value of about –0.003. The predicted data show C_{l_β} decreasing to around –0.006 at 20° AOA and then approaching the flight values at 42° before once again decreasing to –0.005 above 45°. This is a significant disagreement between prediction and flight above 20° AOA in this very important derivative. A primary effect of C_{l_β} is its contribution to the static directional stability of the vehicle. The flight responses show that the vehicle is somewhat less statically stable at high AOA than the original prediction, which is apparent with the flight estimates being less negative (smaller in magnitude) than the predictions.

The flight-determined C_{n_β} (directional stability) in figure 5(b) shows fair agreement with the prediction below 42° AOA, except for the flight being about 70 percent of the predicted value between 10° and 20°. The flight estimates increase as AOA increases from 40° to 48°, and then decrease as AOA increases from 48° to 53°, reaching nearly the predicted value at 53°. Overall, an increased increment is seen in the static directional stability between 45° and 50° AOA for the flight data relative to the prediction. This increment would compensate somewhat for the opposite effect seen for the C_{l_β} contribution.

Figure 5(c) shows good agreement between the flight estimate of C_{Y_β} and the prediction. A somewhat higher value of the flight estimate is seen between 38° and 46° AOA.

The difference between flight and prediction for the sideslip derivatives is significant, but this may be partly because the flight maneuvers were performed at somewhat larger sideslip angles than those used to calculate the predicted values of C_{l_β}, C_{n_β}, and C_{Y_β}. The predicted wind-tunnel values of C_l, C_n, and C_Y are nonlinear functions of β, and, therefore, depend on the amount of β the derivatives are linearized over. In addition, the predicted values of C_{l_β} and C_{n_β} show a dependence on the position settings of the three pairs of longitudinal control surfaces (canards, flaperons, and strakes), which vary in flight with AOA. The sawtooth appearance of the prediction fairings, particularly evident in figures 5(a) and 5(b), is not so much a function of the plotted abscissa (AOA) as it is of the aforementioned differences between flight and prediction concerning angle of sideslip and longitudinal control surface position.

The dominant uncertain effects on the β derivatives at high AOA are caused by vortices emanating from the vehicle nose and the canard and their effects on the aft portions of the vehicle. As is well known, differences in predicted vortex strength and location can lead to discrepancies in the resulting stability derivatives. Combined with scaling, Reynolds number, and dynamic effects, these differences can cause the type of variations between predicted and flight-estimated values of C_{l_β}, C_{n_β}, and C_{Y_β} seen in figures 5(a), 5(b), and 5(c).

Aileron Derivatives

Figure 6(a) shows the aileron effectiveness as a function of AOA. The decreasing trend of the predicted and flight-determined $C_{l_{\delta_a}}$ is similar below 25° AOA, with the flight estimates being lower by up to 0.0005. Above 30° AOA, the predicted value is about half of that determined from flight. The flight-determined roll control power is fairly good all the way to 53°, which is unusual for conventional, aft-swept wings. This good effectiveness could result from a combination of the FSW and the strong flow off the canard that is just ahead of the wing. This resulting effectiveness provides the pilot enhanced ability to hold a bank angle and improved closed-loop damping-in-roll due to the high-gain control system working through the good control effectiveness.

The flight estimates in figure 6(b) show more adverse yaw (less positive $C_{n_{\delta_a}}$) than was predicted above 10° AOA except between 25° and 35°. The $C_{n_{\delta_a}}$ derivative is important in the precise coordination of aileron and rudder for the pilot and in gain selection for designing the high-gain FCS.

Figure 6(c) shows $C_{Y_{\delta_a}}$ for the predicted and flight values. Above 20° AOA, the flight $C_{Y_{\delta_a}}$ varies up to five times the value of the prediction—a large difference for this relatively unimportant derivative.

Rudder Derivatives

The values of $C_{l_{\delta_r}}$ shown in figure 7(a) are positive for all AOA for both predicted and flight. In particular, flight values are higher than predicted values for most of the AOA range. The flight value is substantial between 30° and 45°AOA, while the predictions are near zero. For the three flight points above 50° AOA, $C_{l_{\delta_r}}$ was fixed at zero (and therefore not shown on the $C_{l_{\delta_r}}$ derivative plot) to enable better analysis of the other stability and control derivatives.

Figure 7(b) shows the rudder effectiveness $C_{n_{\delta_r}}$ with the flight values showing more effectiveness (a more negative value) throughout the AOA range, with both going to zero at 50° AOA. For the three maneuvers above 50°, $C_{n_{\delta_r}}$ was fixed at zero to enhance the analysis of those maneuvers. The flight value is about 0.0004 more negative than the predicted value below 42° with lesser differences at higher AOA. The yaw control resulting from the high flight effectiveness is quite adequate up to 40°AOA.

Figure 7(c) shows the predicted and flight values for $C_{Y_{\delta_r}}$. Good agreement is seen between the two throughout the AOA range. The flight values are higher for AOA between 35° and 45°. For the three points above 50° AOA, $C_{Y_{\delta_r}}$ was fixed to zero for the reasons discussed earlier.

Rotary Derivatives

The X-29A number 2 has a very high gain feedback control system which, along with the good aileron and rudder effectiveness, greatly augments the natural aerodynamic damping of the aircraft. The response from a pilot doublet input therefore results in relatively low angular rates that appear to quickly damp the dutch-roll mode (fig. 4). This damping poses two problems in the analysis of the stability and control maneuvers:

1. As shown in figure 4(b), the rates are near zero except when the control surfaces are actually moved, which gives little information for estimating the rotary (or rate) derivatives.

2. The rates are being fed back to the control surfaces, resulting in a high correlation (linear dependence) between the rates (fig. 4(c)) and the control positions. Reference 17 discussed this issue at more length.

Because of these two problems, a low *a priori* weighting (ref. 33) is used on the rotary derivatives to keep the flight-estimated values near the predicted values unless a different value is strongly indicated. If there is no new information, the flight estimate will be the same as the predicted value. If there is some independent information, the flight value will be different than the prediction. The *a priori* weighted values keep the estimation program from using ridiculous estimations of the rotary derivatives to get a better match, that is, a lower value of J (eq. 13). Therefore, a low *a priori* weighting is used on the analysis for maneuvers above 15° AOA.

Figure 8(a) shows the very important damping-in-roll derivative C_{l_p} for the predicted and flight values. Excellent agreement is seen below 18° AOA. The flight estimates show lower damping (less negative values) between 20° and 38°AOA. The fair agreement above 40° AOA still shows some correlation between prediction and flight. Despite the apparent agreement, significant scatter in the flight data indicates the program is not using the exact predicted values. The cluster of three flight estimates between 42° and 43° AOA have relatively small uncertainty levels, indicating significant information for C_{l_p} for these maneuvers. These test points were collected near an altitude of 20,000 ft, while the adjacent estimates of C_{l_p} with larger uncertainty levels were obtained from test points near 30,000 ft. Because of the *a priori* weighting, there may not be much new information from the C_{l_p} estimates that have larger uncertainties.

Figures 8(b), 8(c), and 8(d) for C_{l_r}, C_{n_p}, and C_{n_r} show differences between flight and prediction below 15° AOA where there is no *a priori* weighting, thus indicating new information. The differences above 15° AOA for the relatively small C_{l_r} and C_{n_p} may or may not be new information as discussed earlier. The predicted and flight values for C_{n_r} in figure 8(d) agree above 25° AOA. Coupled with the relatively small values of yaw rate r for the stability and control maneuvers, this indicates very little was learned about C_{n_r} in this AOA.

Aerodynamic and Instrumentation Biases

Figures 9(a), 9(b), and 9(c) show, respectively, the C_{l_0}, C_{n_0}, and C_{Y_0} biases from the PID analysis. The C_{l_0}, C_{n_0}, and C_{Y_0} from the estimation program include any instrumentation biases as well as aerodynamic biases, so they may vary slightly from flight to flight. The apparent aerodynamic biases commonly seen in stability and control analyses at low AOA usually result from the vehicle being somewhat asymmetrical. Also, a small calibration error in the control positions, not uncommon, will typically result in a small value in the biases to zero the steady portion of the maneuver. This small error may vary from flight to flight. The bias values below 15° AOA are probably caused by the two sources of bias just discussed: aircraft asymmetry and calibration error (or instrumentation bias). Above 20° AOA, the X-29A

configuration starts to develop vortex flow that, if asymmetric for any reason, has an additional contribution to C_{l_0} and C_{n_0}. The peak in values for C_{l_0}, C_{n_0}, and C_{Y_0} at 47° AOA is likely caused by significant asymmetric flow from the nose (forebody) vortices. Then, above 50° AOA, the signs of the C_{l_0} and C_{n_0} biases change and their magnitudes increase. This change is probably caused by the sense of the asymmetric vortices switching sides; this is a known problem with the F-5A nose section used on the X-29A number 2.

CONCLUDING REMARKS

This paper presents parameter identification (PID) results based on 52 different PID maneuvers flown by the second X-29A research aircraft during flights 6 to 30 from October 1989 to March 1990 and flights 117, 118, and 120 in September 1991. These efforts supported the flight envelope expansion phase of the second X-29A by providing flight-determined values of the aircraft's lateral–directional stability and control derivatives. The derivatives were used to update the aero model, improve the real-time simulator, and revise flight control system control laws. In addition, the results of this study underscore the important correlation between ground-based predictive techniques and actual flight performance, in turn providing an evaluation of the design methods originally used to develop the aircraft.

The stability and control derivatives reported here were extracted from flight data using a specialized NASA Dryden-developed parameter estimation program. The program uses the linearized aircraft equations of motion and the maximum likelihood estimation method with state noise effects. State noise is used to model the uncommanded forcing function caused by unsteady aerodynamics (separated and vortex flows) over the aircraft at high-angle of attack.

The derivative results are plotted as functions of angle of attack ranging from 4° to 53°, and compared with the predicted preflight AERO9B database. Agreement is good for some derivatives, such as the coefficient of lateral force due to sideslip (C_{Y_β}), the coefficient of lateral force due to rudder deflection ($C_{Y_{\delta_r}}$), and the coefficient of rolling moment due to roll rate (C_{l_p}). The plots also show significant differences in several important derivatives from the predicted aero model. Flight values of the coefficient of rolling moment due to sideslip (C_{l_β}) are quite different from prediction for most of the angle-of-attack range, except for some agreement at the lowest end. Large differences also exist with the coefficient of yawing moment due to sideslip (C_{n_β}) at angles of attack above 40°. The flight-extracted coefficient of yawing moment due to aileron deflection ($C_{n_{\delta_a}}$), which influences the critical coordination of aileron and rudder, shows more adverse yaw than predicted. In addition, flight estimates of the coefficient of yawing moment due to rudder deflection ($C_{n_{\delta_r}}$) are higher than predicted up to 45° angle of attack.

Dryden Flight Research Center
National Aeronautics and Space Administration
Edwards, California, July 1996

REFERENCES

1. Sefic, Walter J., and Cleo M. Maxwell, *X-29A Technology Demonstrator Flight Test Program Overview*, NASA TM-86809, May 1986.

2. Hicks, John W., and Neil W. Matheny, *Preliminary Flight Assessment of the X-29A Advanced Technology Demonstrator*, NASA TM-100407, Sept. 1987.

3. Budd, Gerald D., and Neil W. Matheny, *Preliminary Flight Derived Aerodynamic Characteristics of the X-29A Aircraft Using Parameter Identification Techniques*, NASA TM-100453, Nov. 1988.

4. Trippensee, Gary, and Stephen Ishmael, "Overview of the X-29 High-Angle-of-Attack Program," *High-Angle-of-Attack Technology, Volume I*, NASA CP-3149 Part 1, Joseph R. Chambers, William P. Gilbert, and Luat T. Nguyen, Ed., NASA Langley Research Center, Hampton, Virginia, May 1992, pp. 61–68.

5. Saltzman, Edwin J., and John W. Hicks, *In-Flight Lift-Drag Characteristics for a Forward-Swept Wing Aircraft (and Comparisons With Contemporary Aircraft)*, NASA TP-3414, Dec. 1994.

6. Pellicano, Paul, Joseph Krumenacker, and David Vanhoy, "X-29 High Angle-of-Attack Flight Test Procedures, Results, and Lessons Learned," *Proc. SFTE 21st Ann. Symp.*, Garden Grove, California, Aug. 6–10, 1990, pp. 2.4.1–2.4.23.

7. Smith, Wade R., Capt., USAF, "X-29 High Angle of Attack Flight Test Program, Volume 5—X-29-2 High Angle-of-Attack Flight Test Results," WL-TR-93-3124, Nov. 1993. (Distribution authorized to U.S. Government agencies and their contractors; other requests shall be referred to WL/FIMS, Wright-Patterson AFB, Ohio 45433-6503.)

8. Webster, Fredrick R., and Major Dana Purifoy, USAF, "X-29 High Angle-of-Attack Flying Qualities," AFFTC-TR-91-15, June 1991. (Distribution authorized to U.S. Government agencies and their contractors; other requests shall be referred to WL/FIMT, Wright-Patterson AFB, Ohio 45433-6503.)

9. Bauer, Jeffrey E., Robert Clarke, and John J. Burken, *Flight Test of the X-29A at High Angle of Attack: Flight Dynamics and Controls*, NASA TP-3537, Feb. 1995.

10. Clarke, Robert, John J. Burken, John T. Bosworth, and Jeffrey E. Bauer, *X-29 Flight Control System: Lessons Learned*, NASA TM-4598, June 1994.

11. Earls, Michael R., and Joel R. Sitz, *Initial Flight Qualification and Operational Maintenance of X-29A Flight Software*, NASA TM-101703, Sept. 1989.

12. Fisher, David F., David M. Richwine, and Stephen Landers, *Correlation of Forebody Pressures and Aircraft Yawing Moments on the X-29A Aircraft at High Angles of Attack*, NASA TM-4417, Nov. 1992.

13. Webster, Fred, Mark Croom, and Robert Curry, "Correlation of Ground-Based and Full Scale Flight Results on Aerodynamics and Flight Dynamics of the X-29," High Angle-of-Attack Technology - Volume I, NASA CP-3149 Part 1, pp. 279–303.

14. Clarke, Robert, John Burken, Jeffery Bauer, Michael Earls, Donna Knighton, David McBride, and Fred Webster, *Development and Flight Test of the X-29A High Angle-of-Attack Flight Control System*, NASA TM-101738, Feb. 1991.

15. Cohen, Dorothea, and Jeanette H. Le, *The Role of the Remotely Augmented Vehicle (RAV) Laboratory in Flight Research*, NASA TM-104235, Sept. 1991.

16. Rajczewski, David M., Capt., USAF, "X-29A High Angle-of-Attack Flight Test: Air Data Comparisons of an Inertial Navigation System and Noseboom Probe," *Proc. SFTE 21st Ann. Symp.*, Garden Grove, California, Aug. 6–10, 1990, pp. 4.5.1 –4.5.12.

17. Iliff, Kenneth W., and Richard E. Maine, *Practical Aspects of Using a Maximum Likelihood Estimation Method to Extract Stability and Control Derivatives From Flight Data*, NASA TN D-8209, April 1976.

18. Whipple, Raymond D., and Jonathan L. Ricket, *Low-Speed Aerodynamic Characteristics of a 1/8-Scale X-29A Airplane Model at High Angles of Attack and Sideslip*, NASA TM-87722, Sept. 1986.

19. Murri, Daniel G., Luat T. Nguyen, and Sue B. Grafton, *Wind-Tunnel Free-Flight Investigation of a Model of a Forward-Swept-Wing Fighter Configuration*, NASA TP-2230, Feb. 1984.

20. Croom, Mark A., Raymond D. Whipple, Daniel G. Murri, Sue B. Grafton, and David J. Fratello, "High-Alpha Flight Dynamics Research on the X-29 Configuration Using Dynamic Model Test Techniques," SAE-881420, Oct. 3, 1988.

21. Ralston, John N., *Rotary Balance Data and Analysis for the X-29A Airplane for an Angle-of-Attack Range of 0° to 90°*, NASA CR-3747, 1984.

22. Fratello, David J., Mark A. Croom, Luat T. Nguyen, and Christopher S. Domack, "Use of the Updated NASA Langley Radio-Controlled Drop-Model Technique for High-Alpha Studies of the X-29A Configuration," AIAA-87-2559, Aug. 17, 1987.

23. Raney, David L., and James G. Batterson, *Lateral Stability Analysis for X-29A Drop Model Using System Identification Methodology*, NASA TM-4108, June 1989.

24. Grafton, S. B., W. P. Gilbert, M. A. Croom, and D. G. Murri, "High-Angle-of-Attack Characteristics of a Forward-Swept Wing Fighter Configuration," AIAA-82-1322, Aug. 1982.

25. O'Connor, Cornelius, John Ralston, and Billy Bernhart, *An Incremental Rotational Aerodynamic Math Model of the X-29 Airplane From 0° Through 90° Angle-of-Attack*, AFWAL-TR-88-3067, Sept. 1988.

26. Krumenacker, J., "Revised X-29 High Angle of Attack, Flexible Aerodynamic Math Model (AERO9B); Equations, Computer Subroutines, and Data Tables," GASD 712/ENG-M-88-054, Grumman Aircraft Systems Division, Bethpage, New York, July 14, 1988.

27. Klein, Vladislav, Brent R. Cobleigh, and Keith D. Noderer, *Lateral Aerodynamic Parameters of the X-29 Aircraft Estimated From Flight Data at Moderate to High Angles of Attack*, NASA TM-104155, Dec. 1991.

28. Krumenacker, J., P. Pellicano, and Capt. F. Luria, "X-29 High Angle-of-Attack Flight Test Program: Volume 4—X-29 High Angle-of-Attack Aero Model Evolution," WL-TR-93-3121, Oct. 1993. (Distribution authorized to U.S. Government agencies and their contractors; other requests shall be referred to WL/FIMS Wright-Patterson AFB, Ohio 45433-6503)

29. Iliff, Kenneth W., Richard E. Maine, and Mary Shafer, *Subsonic Stability and Control Derivatives for an Unpowered, Remotely Piloted 3/8-Scale F-15 Airplane Model Obtained from Flight Test,* NASA TN D-8136, Jan. 1976.

30. Iliff, Kenneth W., "Identification and Stochastic Control with Application to Flight Control in Turbulence," UCLA-ENG-7430, Ph.D. Dissertation, Univ. of California Los Angeles, California, May 1973.

31. Maine, R. E., and K. W. Iliff, *Identification of Dynamic Systems*, AGARD-AG-300, vol. 2, Jan. 1985. (Also available as NASA RP-1138, Feb. 1985.)

32. Iliff, Kenneth W., "Identification and Stochastic Control of an Aircraft Flying in Turbulence," *J. Guidance and Control*, vol. 1, no. 2, March–April 1978, pp. 101–108.

33. Iliff, Kenneth W., and Lawrence W. Taylor, Jr., *Determination of Stability Derivatives From Flight Data Using a Newton-Raphson Minimization Technique*, NASA TN D-6579, March 1972.

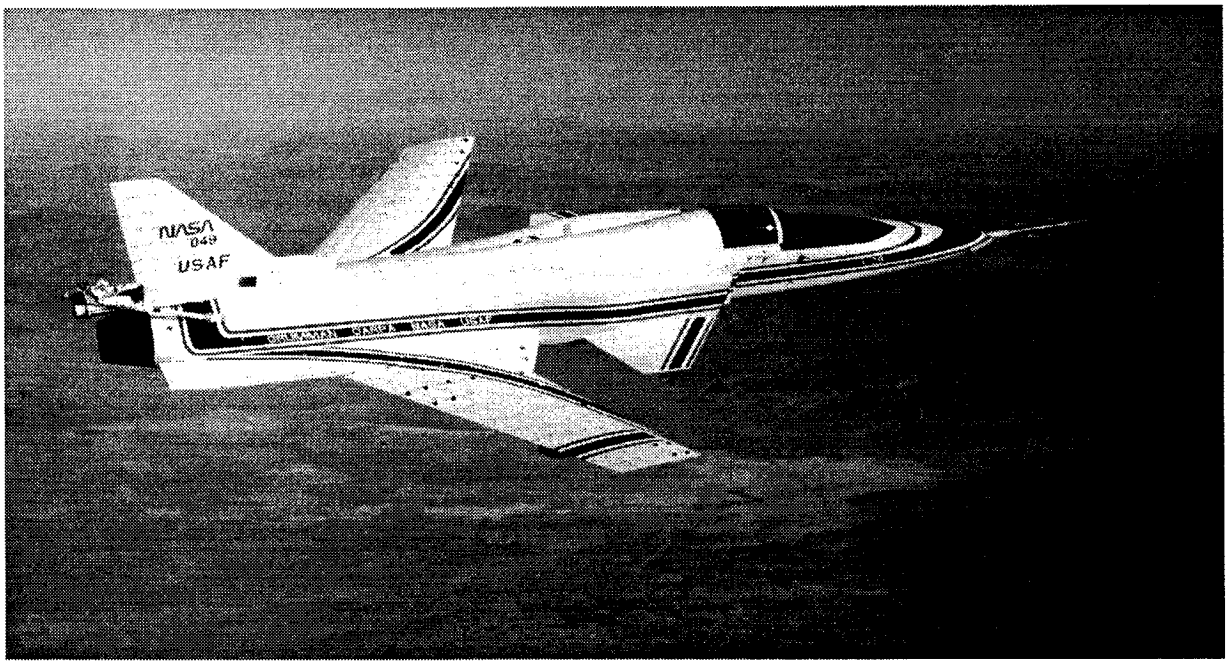

EC 90-48-16

Figure 1. X-29A aircraft, number 2.

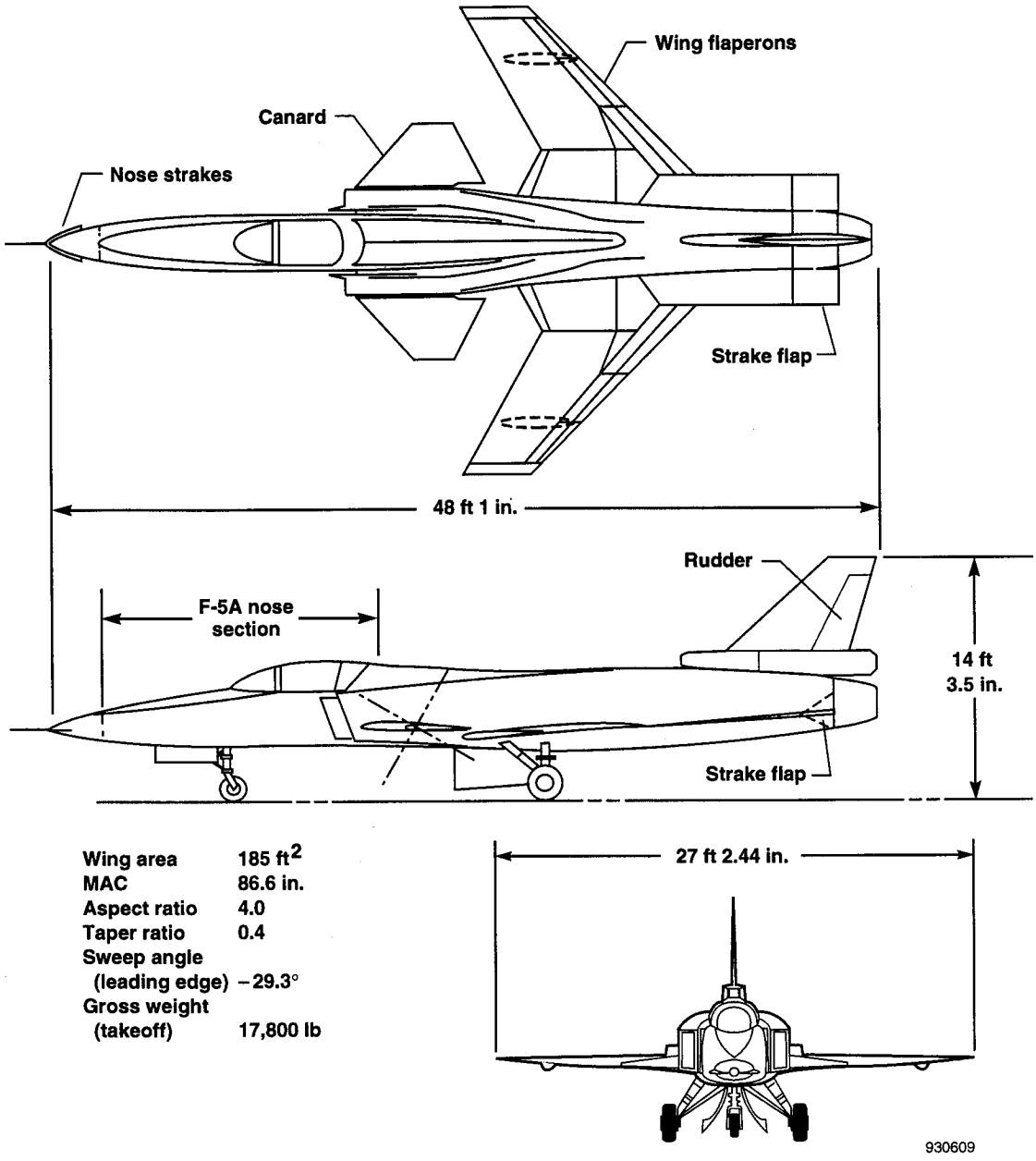

Figure 2. Three-view drawing of the X-29A showing major dimensions.

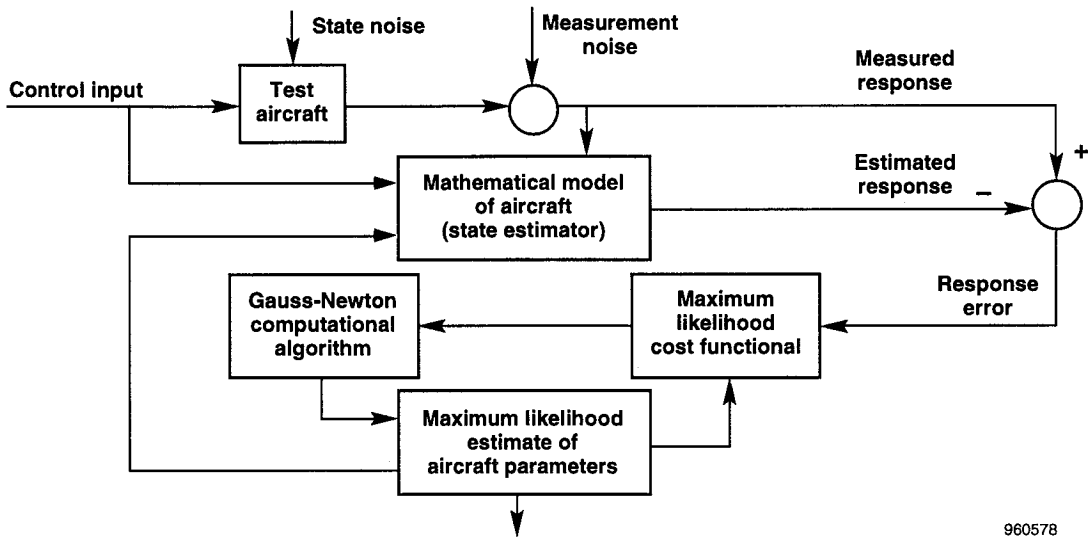

Figure 3. The maximum likelihood estimation concept with state and measurement noise.

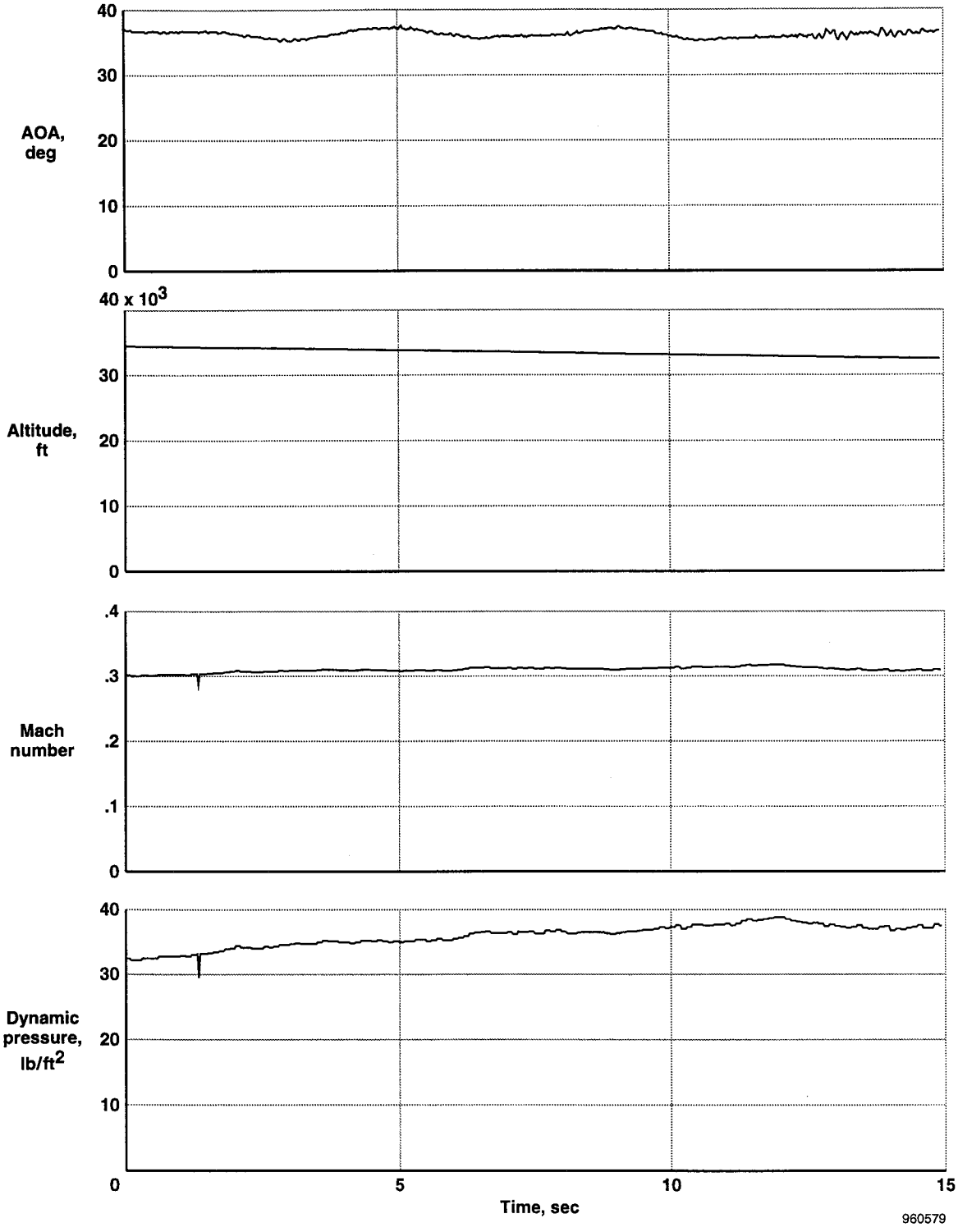

(a)

Figure 4. Time-history data for a typical high-AOA, lateral–directional, PID maneuver.

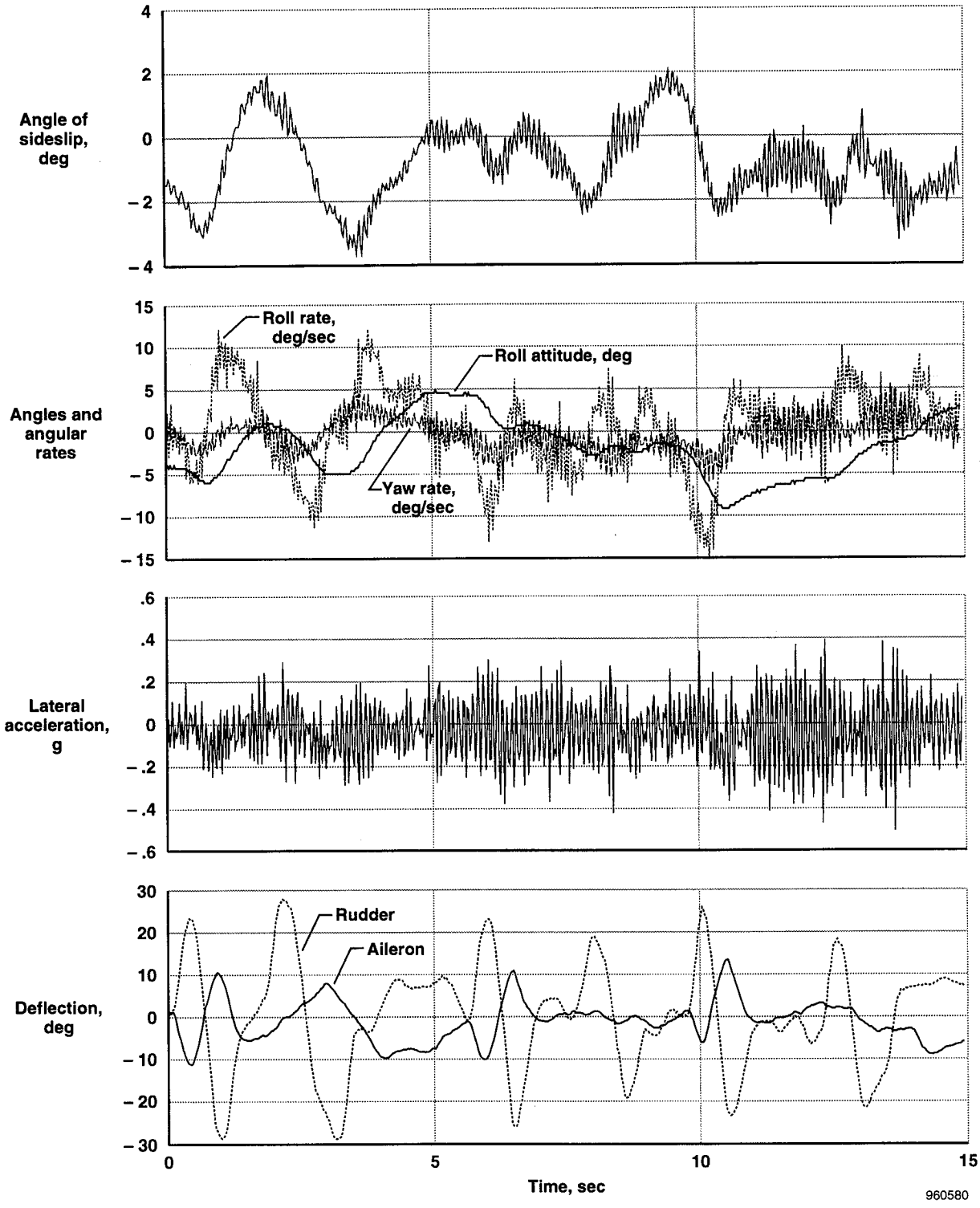

(b)

Figure 4. Continued.

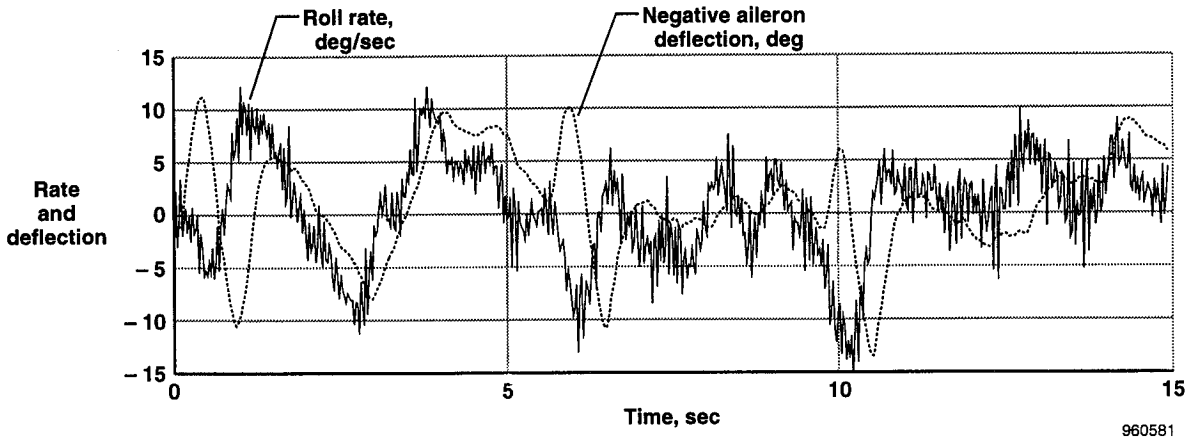

(c)

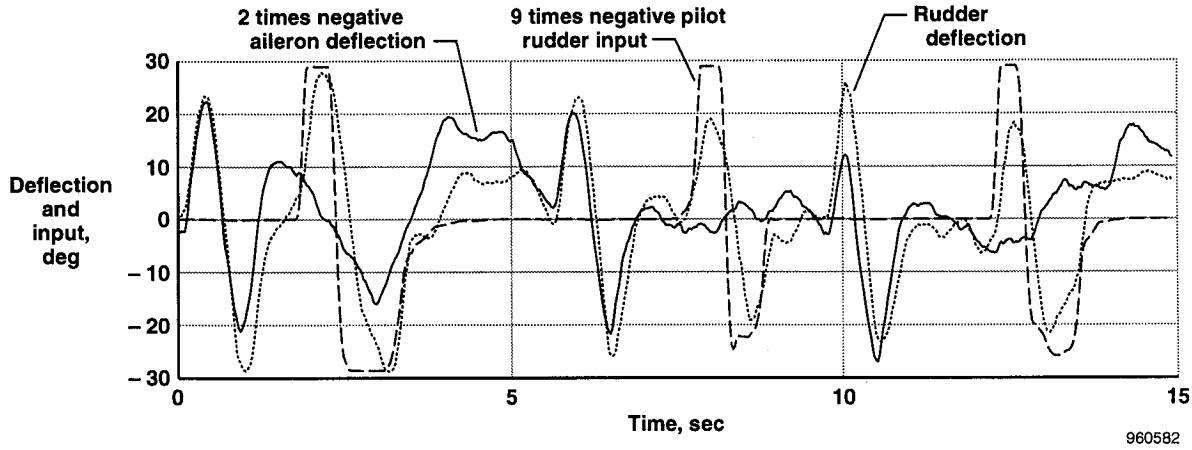

(d)

Figure 4. Concluded.

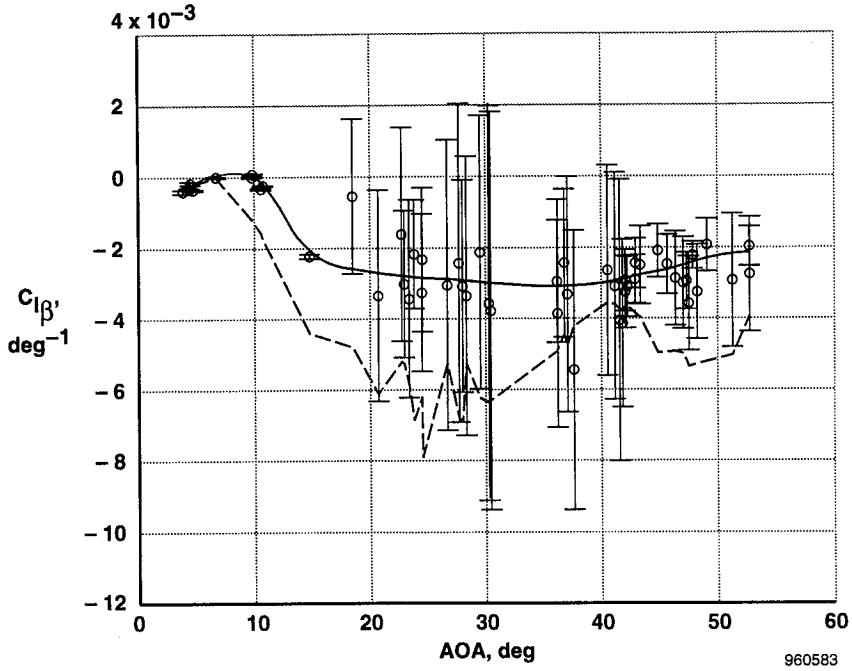

(a) C_{l_β} as a function of AOA.

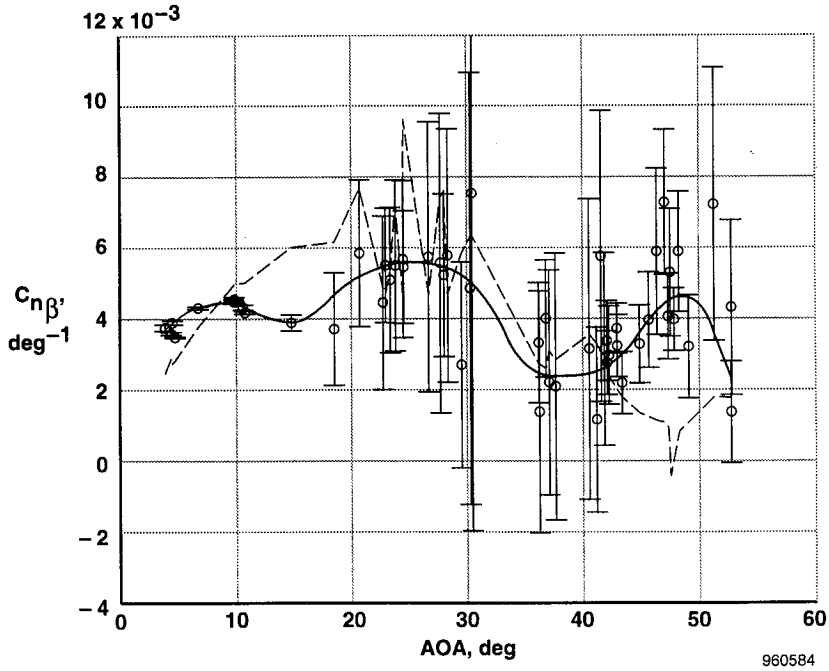

(b) C_{n_β} as a function of AOA.

Figure 5. Sideslip derivatives as functions of AOA.

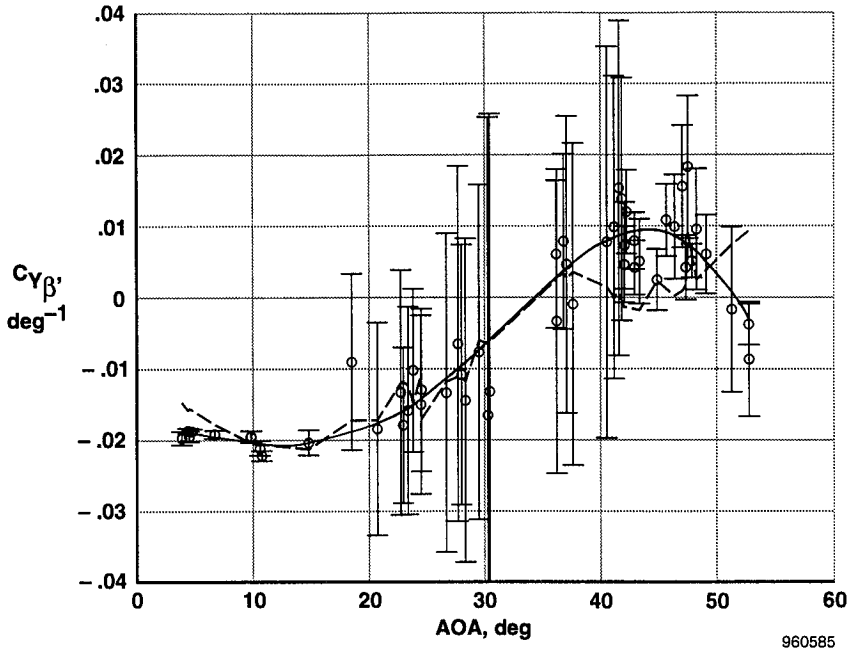

(c) C_{Y_β} as a function of AOA.

Figure 5. Concluded.

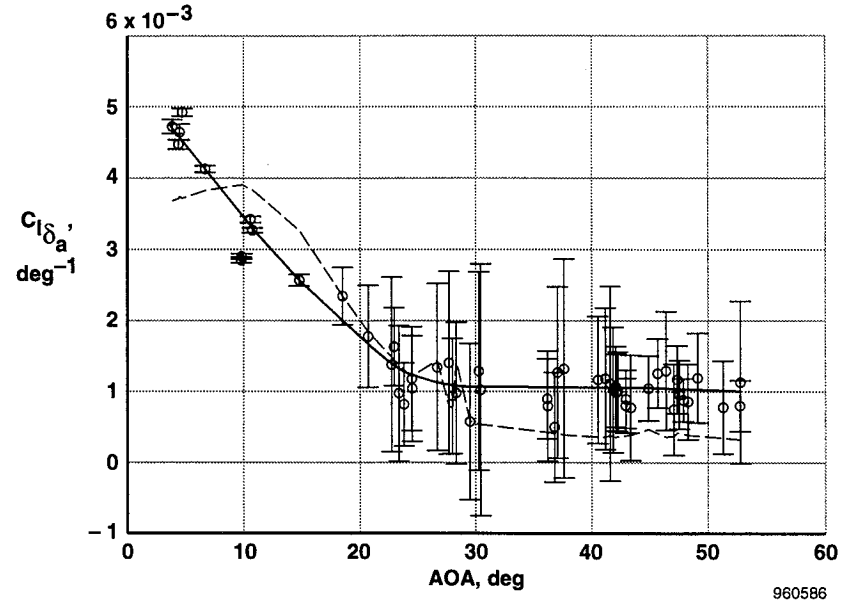

(a) $C_{l_{\delta_a}}$ as a function of AOA.

Figure 6. Aileron derivatives as functions of AOA.

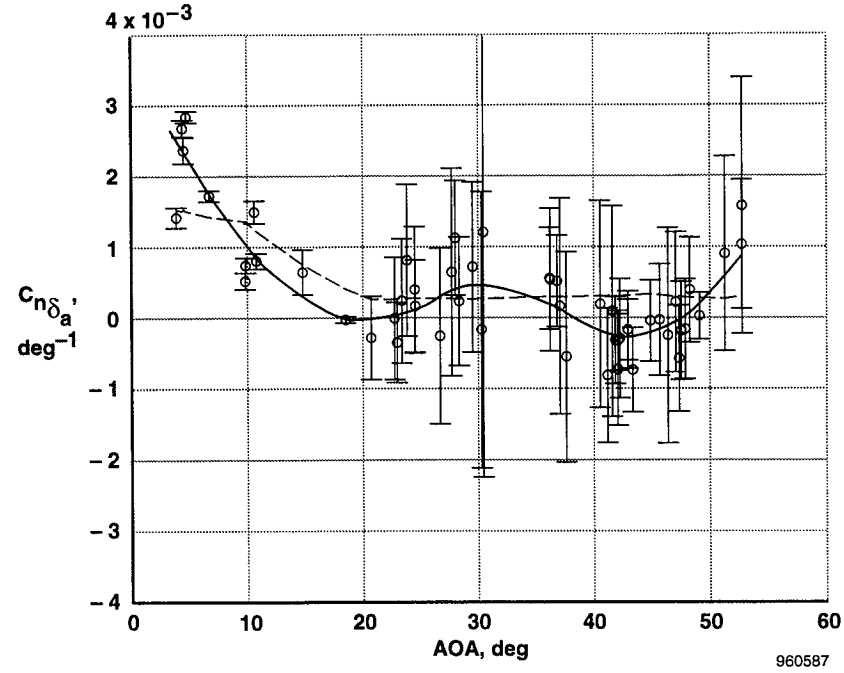

(b) $C_{n_{\delta_a}}$ as a function of AOA.

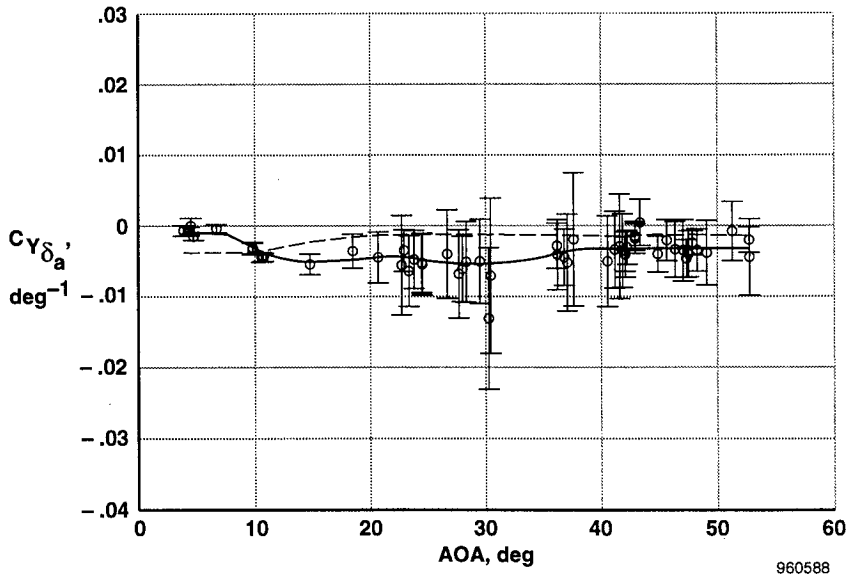

(c) $C_{Y_{\delta_a}}$ as a function of AOA.

Figure 6. Concluded.

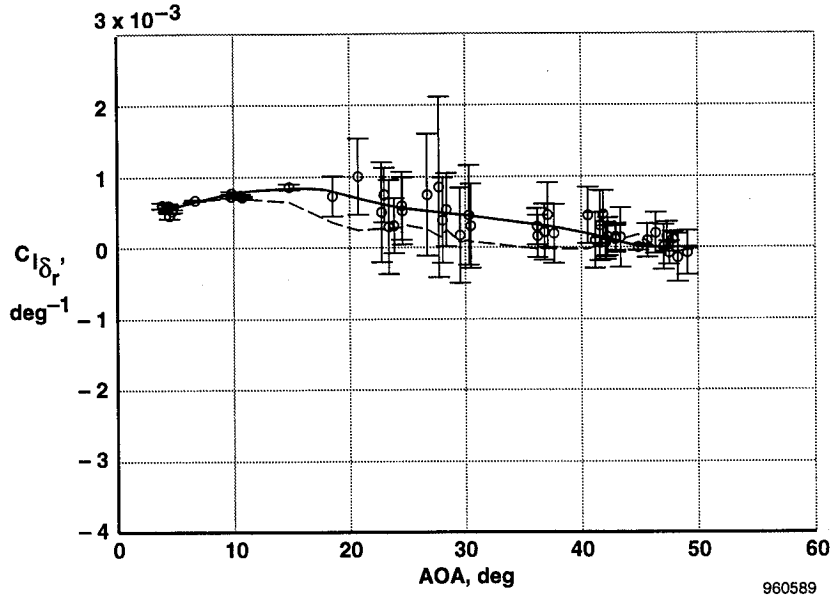

(a) $C_{l_{\delta_r}}$ as a function of AOA.

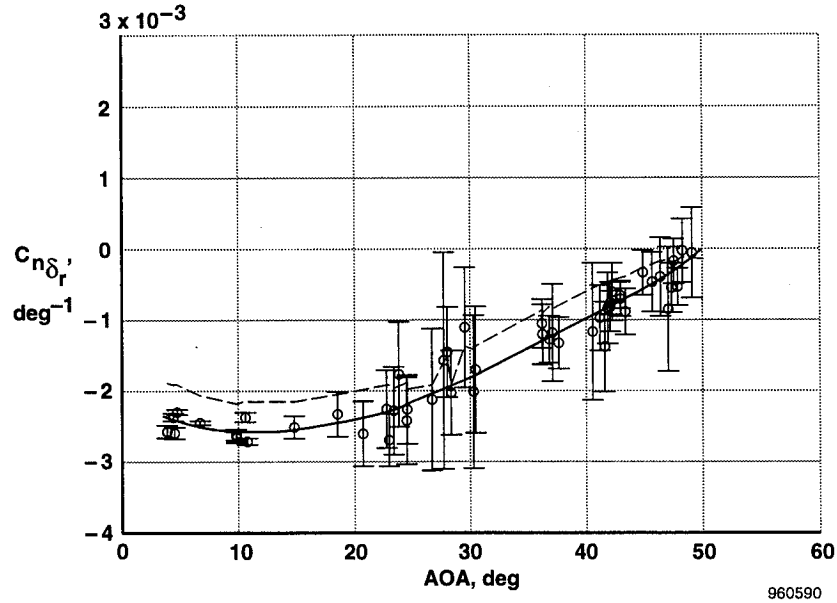

(b) $C_{n_{\delta_r}}$ as a function of AOA.

Figure 7. Rudder derivatives as functions of AOA.

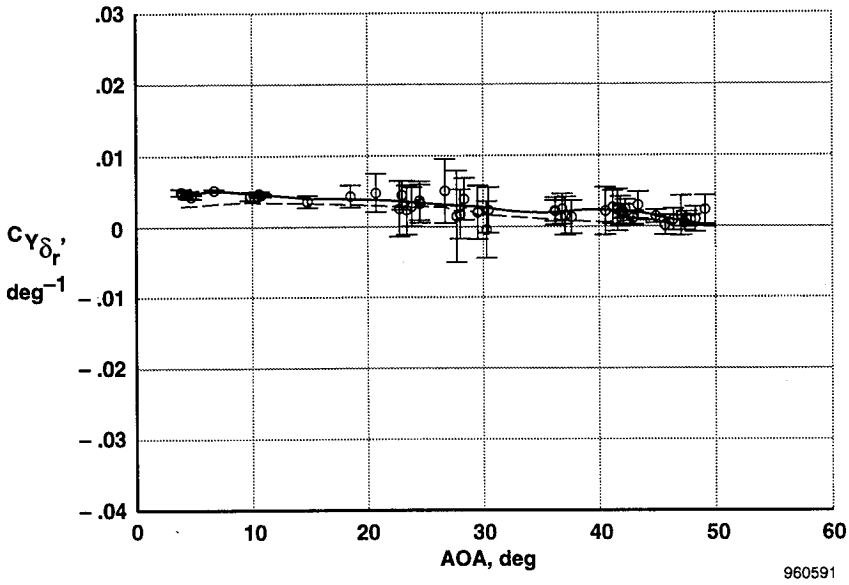

(c) $C_{Y_{\delta_r}}$ as a function of AOA.

Figure 7. Concluded.

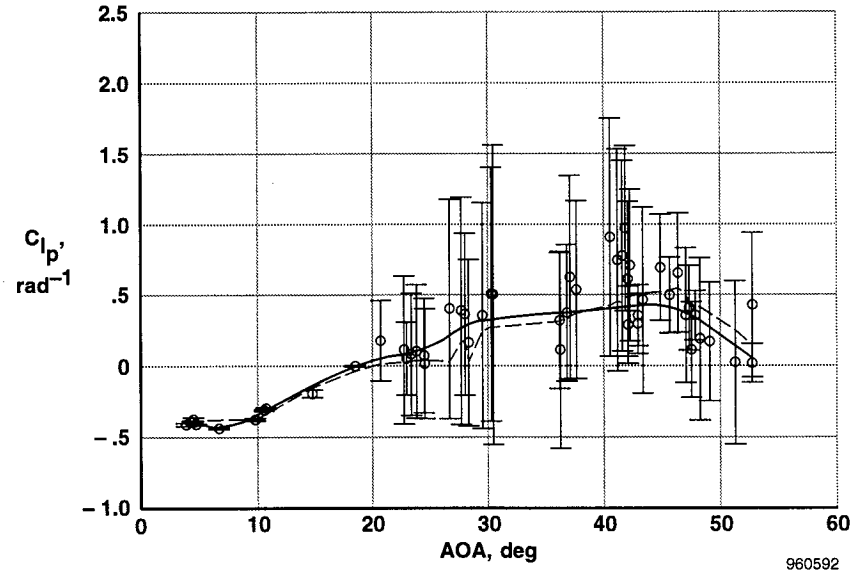

(a) C_{l_p} as a function of AOA.

Figure 8. Rotary derivatives as functions of AOA.

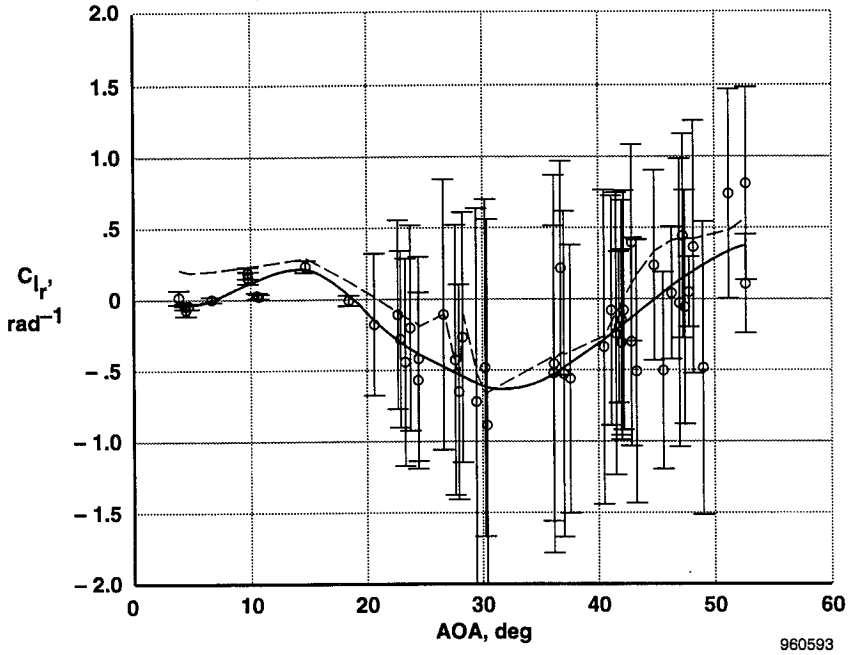

(b) C_{l_r} as a function of AOA.

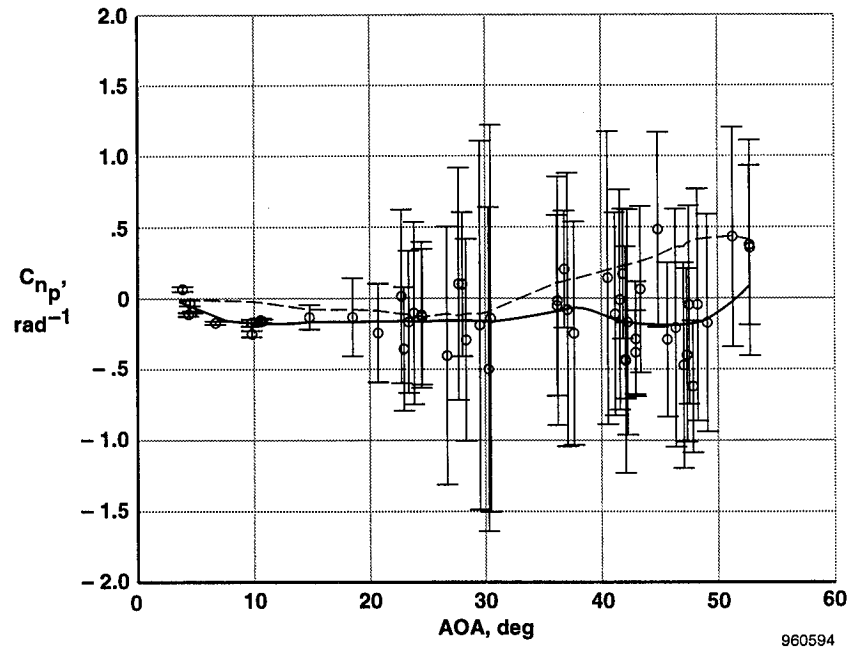

(c) C_{n_p} as a function of AOA.

Figure 8. Continued.

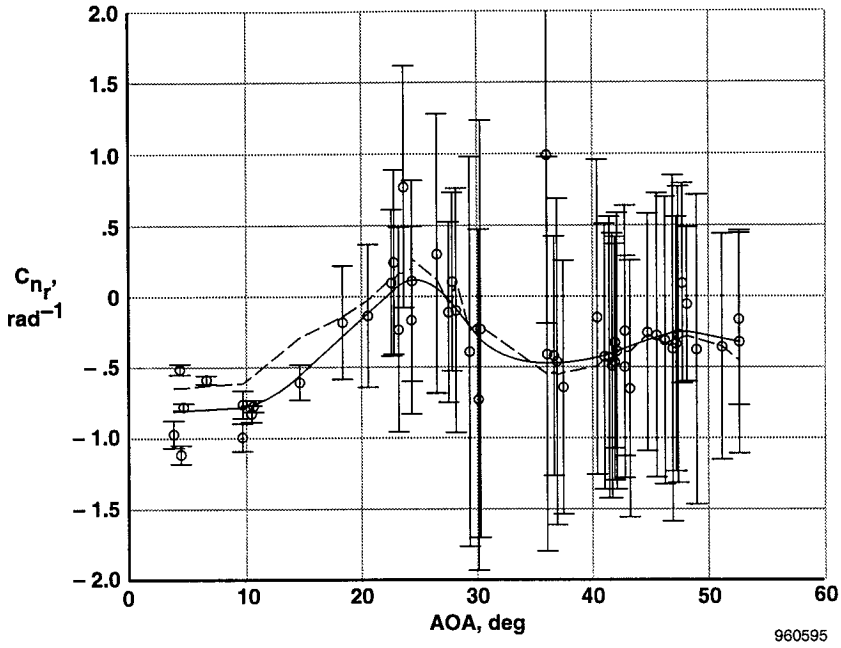

(d) C_{n_r} as a function of AOA.

Figure 8. Concluded.

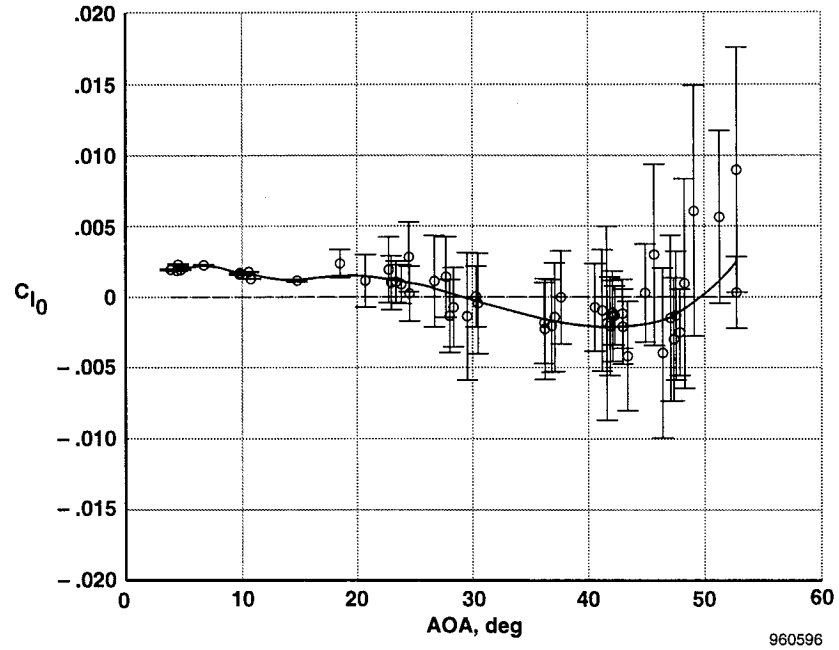

(a) C_{l_0} as a function of AOA.

Figure 9. Aerodynamic and instrumentation biases as functions of AOA.

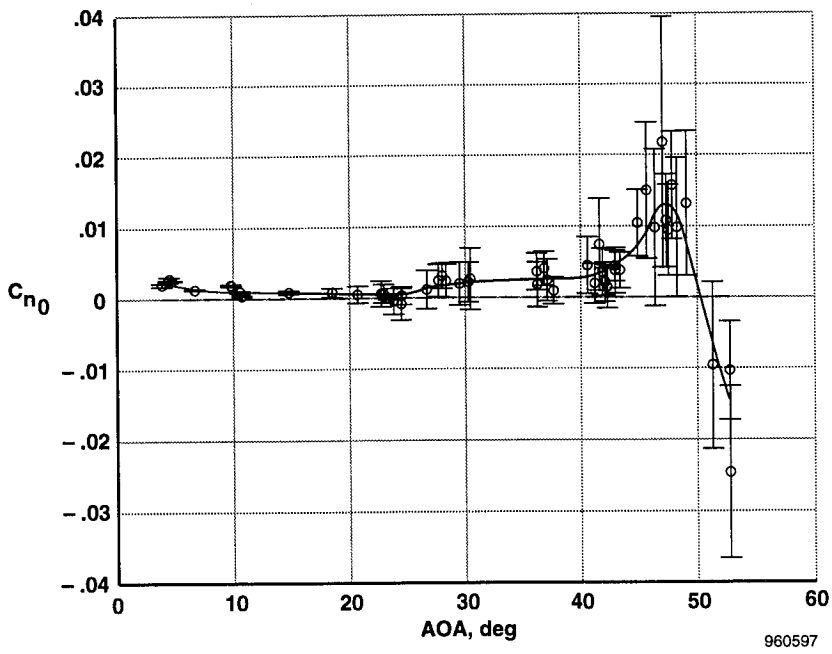

(b) C_{n_0} as a function of AOA.

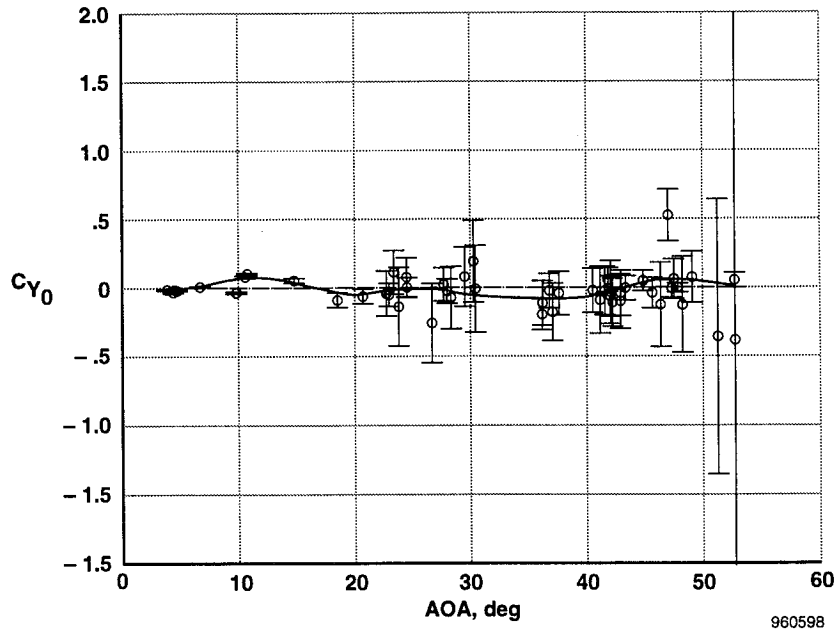

(c) C_{Y_0} as a function of AOA.

Figure 9. Concluded.

REPORT DOCUMENTATION PAGE

Form Approved
OMB No. 0704-0188

1. AGENCY USE ONLY (Leave blank)	2. REPORT DATE	3. REPORT TYPE AND DATES COVERED
	December 1996	Technical Paper

4. TITLE AND SUBTITLE

X-29A Lateral–Directional Stability and Control Derivatives Extracted From High-Angle-of-Attack Flight Data

5. FUNDING NUMBERS

WU 505 68 50 00R

6. AUTHOR(S)

Kenneth W. Iliff and Kon-Sheng Charles Wang

7. PERFORMING ORGANIZATION NAME(S) AND ADDRESS(ES)

NASA Dryden Flight Research Center
P.O. Box 273
Edwards, California 93523-0273

8. PERFORMING ORGANIZATION REPORT NUMBER

H-2118

9. SPONSORING/MONITORING AGENCY NAME(S) AND ADDRESS(ES)

National Aeronautics and Space Administration
Washington, DC 20546-0001

10. SPONSORING/MONITORING AGENCY REPORT NUMBER

NASA TP-3664

11. SUPPLEMENTARY NOTES

12a. DISTRIBUTION/AVAILABILITY STATEMENT

Unclassified—Unlimited
Subject Category 08

12b. DISTRIBUTION CODE

13. ABSTRACT (Maximum 200 words)

The lateral–directional stability and control derivatives of the X-29A number 2 are extracted from flight data over an angle-of-attack range of 4° to 53° using a parameter identification algorithm. The algorithm uses the linearized aircraft equations of motion and a maximum likelihood estimator in the presence of state and measurement noise. State noise is used to model the uncommanded forcing function caused by unsteady aerodynamics over the aircraft at angles of attack above 15°. The results supported the flight-envelope-expansion phase of the X-29A number 2 by helping to update the aerodynamic mathematical model, to improve the real-time simulator, and to revise flight control system laws. Effects of the aircraft high gain flight control system on maneuver quality and the estimated derivatives are also discussed. The derivatives are plotted as functions of angle of attack and compared with the predicted aerodynamic database. Agreement between predicted and flight values is quite good for some derivatives such as the lateral force due to sideslip, the lateral force due to rudder deflection, and the rolling moment due to roll rate. The results also show significant differences in several important derivatives such as the rolling moment due to sideslip, the yawing moment due to sideslip, the yawing moment due to aileron deflection, and the yawing moment due to rudder deflection.

14. SUBJECT TERMS	15. NUMBER OF PAGES
Aerodynamic characteristics; Forward-swept wing; High angle of attack; Lateral-directional; Maximum likelihood estimation; Parameter identification; Stability and control derivatives; X-29A	40
	16. PRICE CODE: A03

17. SECURITY CLASSIFICATION OF REPORT	18. SECURITY CLASSIFICATION OF THIS PAGE	19. SECURITY CLASSIFICATION OF ABSTRACT	20. LIMITATION OF ABSTRACT
Unclassified	Unclassified	Unclassified	Unlimited

NSN 7540-01-280-5500

Available from the NASA Center for AeroSpace Information, 800 Elkridge Landing Road, Linthicum Heights, MD 21090; (301)621-0390

Standard Form 298 (Rev. 2-89)
Prescribed by ANSI Std. Z39-18
298-102